

# Atomically accurate de novo design of antibodies with RFdiffusion

<https://doi.org/10.1038/s41586-025-09721-5>

Received: 25 February 2025

Accepted: 8 October 2025

Published online: 5 November 2025

Open access

 Check for updates

Nathaniel R. Bennett<sup>1,2,3,21</sup>, Joseph L. Watson<sup>1,2,21✉</sup>, Robert J. Ragotte<sup>1,2,21✉</sup>, Andrew J. Borst<sup>1,2,21</sup>, DéJenaé L. See<sup>1,2,4,21</sup>, Connor Weidle<sup>1,2,21</sup>, Riti Biswas<sup>1,2,3,21</sup>, Yutong Yu<sup>5,6,7,21</sup>, Ellen L. Shrock<sup>1,2</sup>, Russell Ault<sup>8,9</sup>, Philip J. Y. Leung<sup>1,3</sup>, Buwei Huang<sup>1,2,4</sup>, Inna Goreshnik<sup>1,2,10</sup>, John Tam<sup>11</sup>, Kenneth D. Carr<sup>12</sup>, Benedikt Singer<sup>1,2</sup>, Cameron Criswell<sup>1,2</sup>, Basile I. M. Wicky<sup>1,2</sup>, Dionne Vafeados<sup>2</sup>, Mariana Garcia Sanchez<sup>2</sup>, Ho Min Kim<sup>12,13</sup>, Susana Vázquez Torres<sup>1,2,14</sup>, Sidney Chan<sup>2</sup>, Shirley M. Sun<sup>15,16</sup>, Timothy T. Spear<sup>17</sup>, Yi Sun<sup>15,16</sup>, Keelan O'Reilly<sup>17</sup>, John M. Maris<sup>9,17</sup>, Nikolaos G. Sgourakis<sup>15,16</sup>, Roman A. Melnyk<sup>11,18</sup>, Chang C. Liu<sup>5,6,19,20</sup> & David Baker<sup>1,2,10✉</sup>

Despite the central role of antibodies in modern medicine, no method currently exists to design novel, epitope-specific antibodies entirely in silico. Instead, antibody discovery currently relies on immunization, random library screening or the isolation of antibodies directly from patients<sup>1</sup>. Here we demonstrate that combining computational protein design using a fine-tuned RFdiffusion<sup>2</sup> network with yeast display screening enables the de novo generation of antibody variable heavy chains (VHHs), single-chain variable fragments (scFvs) and full antibodies that bind to user-specified epitopes with atomic-level precision. We experimentally characterize VHH binders to four disease-relevant epitopes. Cryo-electron microscopy confirms the binding pose of designed VHHs targeting influenza haemagglutinin and *Clostridium difficile* toxin B (TcdB). A high-resolution structure of the influenza-targeting VHH confirms atomic accuracy of the designed complementarity-determining regions (CDRs). Although initial computational designs exhibit modest affinity (tens to hundreds of nanomolar  $K_d$ ), affinity maturation using OrthoRep<sup>3</sup> enables production of single-digit nanomolar binders that maintain the intended epitope selectivity. We further demonstrate the de novo design of scFvs to TcdB and a PHOX2B peptide–MHC complex by combining designed heavy-chain and light-chain CDRs. Cryo-electron microscopy confirms the binding pose for two distinct TcdB scFvs, with high-resolution data for one design verifying the atomically accurate design of the conformations of all six CDR loops. Our approach establishes a framework for the computational design, screening and characterization of fully de novo antibodies with atomic-level precision in both structure and epitope targeting.

Antibodies are the dominant class of protein therapeutics, with over 160 antibody therapeutics currently licensed globally and a market value expected to reach US\$445 billion in the next 5 years<sup>4</sup>. Antibody development generally proceeds in two stages: (1) the discovery of antibodies that bind to a specific epitope; and (2) the subsequent affinity maturation and clinical optimization of those antibodies. Currently, identifying epitope-specific antibodies relies on animal immunization or screening of antibody libraries to identify candidate molecules that

bind to a desired target, followed by subsequent epitope mapping. These methods are laborious, time-consuming and can fail to identify antibodies that interact with the therapeutically relevant epitope<sup>1</sup>. Efforts at computational design of antibodies have generally focused on the second optimization step of antibody development, such as sampling alternative native CDR loops to improve affinities<sup>5,6</sup> or using Rosetta<sup>7</sup> sequence design to improve the interacting regions. More recently, structure-based and sequence-based deep learning networks

<sup>1</sup>Department of Biochemistry, University of Washington, Seattle, WA, USA. <sup>2</sup>Institute for Protein Design, University of Washington, Seattle, WA, USA. <sup>3</sup>Graduate Program in Molecular Engineering, University of Washington, Seattle, WA, USA. <sup>4</sup>Department of Bioengineering, University of Washington, Seattle, WA, USA. <sup>5</sup>Department of Biomedical Engineering, University of California, Irvine, CA, USA. <sup>6</sup>Center for Synthetic Biology, University of California, Irvine, CA, USA. <sup>7</sup>Department of Pharmaceutical Sciences, University of California, Irvine, CA, USA. <sup>8</sup>Department of Pediatrics, Children's Hospital of Philadelphia, Philadelphia, PA, USA. <sup>9</sup>Department of Pediatrics, Perelman School of Medicine at the University of Pennsylvania, Philadelphia, PA, USA. <sup>10</sup>Howard Hughes Medical Institute, University of Washington, Seattle, WA, USA. <sup>11</sup>Molecular Medicine Program, The Hospital for Sick Children, Toronto, Ontario, Canada. <sup>12</sup>Center for Biomolecular and Cellular Structure, Institute for Basic Science (IBS), Daejeon, Republic of Korea. <sup>13</sup>Department of Biological Sciences, Korea Advanced Institute of Science and Technology (KAIST), Daejeon, Republic of Korea. <sup>14</sup>Graduate Program in Biological Physics, Structure and Design, University of Washington, Seattle, WA, USA. <sup>15</sup>Center for Computational and Genomic Medicine, Department of Pathology and Laboratory Medicine, Children's Hospital of Philadelphia, Philadelphia, PA, USA. <sup>16</sup>Department of Biochemistry and Biophysics, University of Pennsylvania, Philadelphia, PA, USA. <sup>17</sup>Division of Oncology and Center for Childhood Cancer Research, Children's Hospital of Philadelphia, Philadelphia, PA, USA. <sup>18</sup>Department of Biochemistry, University of Toronto, Toronto, Ontario, Canada. <sup>19</sup>Department of Chemistry, University of California, Irvine, CA, USA. <sup>20</sup>Department of Molecular Biology & Biochemistry, University of California, Irvine, CA, USA. <sup>21</sup>These authors contributed equally: Nathaniel R. Bennett, Joseph L. Watson, Robert J. Ragotte, Andrew J. Borst, DéJenaé L. See, Connor Weidle, Riti Biswas, Yutong Yu. ✉e-mail: jwatson3@uw.edu; ragotte@uw.edu; dabaker@uw.edu

have been trained to design novel antibody sequence variants<sup>8–10</sup>, but these methods require an initial binding antibody from which to optimize. There have also been recent advances in antibody optimization with deep learning methods trained on data generated by powerful new experimental methods<sup>11,12</sup>. By contrast, computational methods able to perform the first stage of antibody design (generating epitope-specific binding antibodies) do not exist, and *de novo* (no homology to an existing antibody targeting that epitope) design of antibodies therefore remains an unsolved problem. There has been rapid progress in designing binding proteins (not antibodies) using RFdiffusion<sup>2,13,14</sup>. However, as with other methods for *de novo* interface design<sup>15–17</sup>, these binders almost exclusively rely on regular secondary structure-based (helical or strand) interactions with the target epitope, and the original ('vanilla') RFdiffusion network is therefore unable to design antibodies *de novo* (Supplementary Fig. 1; see ref. 18).

An ideal method for designing *de novo* antibodies would enable: (1) targeting of any specified epitope on any target of interest; (2) focusing of sampling on the CDR loops, keeping the framework sequence and structure close to a user-specified highly optimized therapeutic antibody framework; and (3) sampling of alternative rigid-body placements of the designed antibody with respect to the epitope. We hypothesized that a specialized version of RFdiffusion fine-tuned on antibody structures should be capable of designing *de novo* CDR-mediated interfaces, given the diversity and quality of *de novo* interfaces that RFdiffusion can design and given that the underlying thermodynamics of interface formation are the same, and set out to develop such a method.

## Training RFdiffusion for antibody design

RFdiffusion uses the AlphaFold2 (ref. 19) and RF2 frame representation of protein backbones comprising the C $\alpha$  coordinate and N-C $\alpha$ -C rigid orientation for each residue. During training, a noising schedule is used that, over a set number of 'timesteps' ( $T$ ), corrupts the protein frames towards random prior distributions (C $\alpha$  coordinates are corrupted with three-dimensional Gaussian noise, and residue orientations with Brownian motion on SO3). During training, a Protein Data Bank (PDB) structure and a random timestep ( $t$ ) are sampled, and  $t$  noising steps are applied to the structure. RFdiffusion predicts the de-noised ( $pX_0$ ) structure at each timestep, and a mean squared error loss is minimized between the true structure ( $X_0$ ) and the prediction ( $pX_0$ ). At inference time, a random residue distribution ( $X_T$ ) is sampled, and RFdiffusion iteratively de-noises this to generate novel protein structures.

We fine-tuned RFdiffusion predominantly on antibody complex structures (Fig. 1; see Methods in Supplementary Information). At each step of training, the antibody structure is corrupted. To permit specification of the framework structure and sequence at inference time, the framework sequence and structure are provided as conditioning input to RFdiffusion during training (Fig. 1b). Because it is desirable for the rigid-body position (dock) between antibody and target to be designed by RFdiffusion along with the CDR loop conformations, the framework structure is provided in a global-frame-invariant manner during training (Fig. 1c). We utilize the 'template track' of RF2/RFdiffusion to provide the framework structure as a two-dimensional matrix of pairwise distances and dihedral angles between each pair of residues (a representation from which three-dimensional structures can be accurately recapitulated)<sup>20</sup> (Supplementary Fig. 1a). The framework and target templates do not encode their relative positions in the three-dimensional space. In this work, we kept the sequence and structure of the framework region fixed, and focused on the design of the CDRs and the overall rigid-body placement of the antibody to the target. We trained RFdiffusion with an additional one-hot encoded 'hotspot' feature, which provides some fraction of the residues that the antibody CDRs interact with, such that at inference, we can direct antibodies towards a specific site (Fig. 1d; we refer to these sites as

'epitopes' throughout the remainder of the text). For simplicity, we refer to this fine-tuned version of the network as RFdiffusion for the remainder of this paper.

With this training regime, RFdiffusion is able to design antibody structures that closely match the structure of the input framework structure and target the specified epitope with novel CDR loops (Supplementary Fig. 1). After the RFdiffusion step, we use ProteinMPNN to design the CDR loop sequences. The designed antibodies make diverse interactions with the target epitope and differ significantly from sequences in the training dataset (Extended Data Fig. 1). There was no correlation between training dataset similarity and binding success (Extended Data Fig. 1a, red lines).

## Fine-tuning RF2 for antibody validation

Design pipelines typically produce a wide range of solutions to any given design challenge. An effective way to filter designed proteins and interfaces that are most likely to succeed experimentally is based on the similarity of the designed structure to the AlphaFold2-predicted structure for the designed sequence (this is often referred to as 'self-consistency'), which has been shown to correlate well with experimental success<sup>21,22</sup>. In the case of antibodies, however, AlphaFold2 fails to accurately predict antibody–antigen structures<sup>23</sup>, preventing its use as a filter in an antibody design pipeline, and at the outset of this project, AlphaFold3 (ref. 24) was not available.

We sought to improve design filtering by fine-tuning RoseTTAFold2 on antibody structures. To simplify antibody structure prediction, we provided information during training about the structure of the target and the location of the target epitope to which the antibody binds; the fine-tuned RF2 must still correctly model the CDRs and find the correct orientation of the antibody to the targeted region. The rationale for providing this information is that the target structure and binding location are available during design (but are typically not available during general structure prediction). With this training regimen and additional information, RF2 is able to robustly distinguish true antibody–antigen pairs from decoy pairs and often accurately predicts antibody–antigen complex structures, but only when the bound (holo) conformation of the target structure and epitope information is provided (Extended Data Fig. 2a–d). At monomer prediction, the fine-tuned RF2 outperformed previous models available at the time, especially at CDR H3 structure prediction (Extended Data Fig. 2e,f).

When this fine-tuned RF2 network is used to re-predict the structure of RFdiffusion-designed VHHS, a significant fraction are confidently predicted to bind in an almost identical manner to their designed structure (Extended Data Fig. 3a). Furthermore, *in silico* cross-reactivity analyses demonstrated that RFdiffusion-designed VHHS are rarely predicted to bind to unrelated proteins (Extended Data Fig. 3b). VHHS that are confidently predicted to bind to their designed target are predicted to form high-quality interfaces, as measured by Rosetta ddG (Extended Data Fig. 3c). This indicates that RF2 filtering might enrich for experimentally successful binders.

## Design and characterization of VHHS

We initially focused on the design of single-domain antibodies (VHHS) produced by camelids<sup>25</sup>. To date, two VHH-based therapies have been approved by the FDA with many clinical trials ongoing<sup>25</sup>. Despite having fewer CDR loops (three) than conventional antibodies (six), the average interaction surface area of a VHH is very similar to that of an antibody<sup>26</sup>, suggesting that a method capable of VHH design could also be suitable for antibody design. Indeed, *in silico* metrics for scFvs and VHHS showed similar qualities of interfaces, as assessed by Rosetta<sup>7</sup> and fine-tuned RF2 (Extended Data Fig. 3b–f).

We chose a widely used humanized VHH framework (h-NbBcl11OF-GLA)<sup>27</sup> as the basis of our VHH design campaigns, and designed VHHS

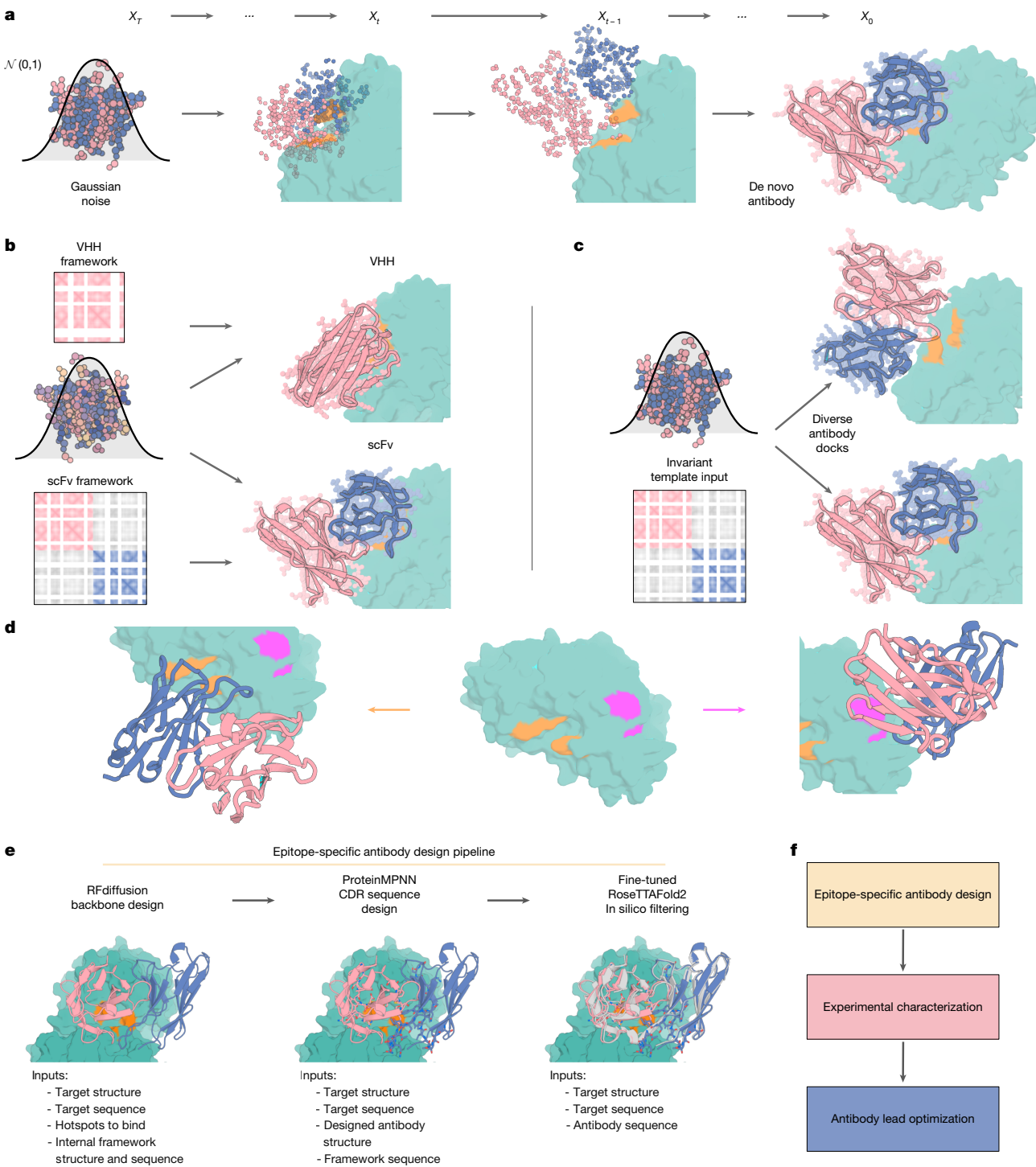


**Fig. 1 | Overview of RFdiffusion for antibody design.** **a**, RFdiffusion is trained such that at time  $T$ , a sample is drawn from the prior distribution (three-dimensional Gaussian distribution for translations and uniform SO<sub>3</sub> distribution for rotations), and de-noised between times  $T$  and 0 to generate an (in this case) scFv. **b**, The antibody framework is provided as a sequence and ‘template’ to RFdiffusion; the latter specifying the pairwise distances and dihedral angles between framework residues. For example, one can specify the design of a VH<sub>H</sub> (top) or scFv (bottom). **c**, Diversity in the antibody–target dock is achieved because the framework template does not encode the rigid body framework–target relationship. Diverse docking modes are sampled by RFdiffusion. **d**, The epitope is specified by provision of ‘hotspot’ residues, which direct the designed antibody (compare orange, left, versus pink, right). **e**, Overview of the computational design pipeline described in this article. RFdiffusion performs the backbone design step, given a target, epitope

hotspots and antibody framework. ProteinMPNN designs only the sequence of the CDR residues (not the framework residues). Fine-tuned RoseTTAFold2 predicts the structure of the designed antibody, given the target (sequence, structure and, optionally, some fraction of hotspot residues) and designed antibody sequence. Self-consistency (high similarity between predicted and designed structures) and high confidence (low predicted alignment error) define in silico success. Note that AlphaFold3, not available at the time of this work, is a better predictor of success than RoseTTAFold2. **f**, The contribution of this work is the epitope-specific antibody design pipeline depicted in panel **e**. Several methods can be used to experimentally validate designs and subsequently affinity-mature or optimize them. In this work, we used yeast surface display and/or *E. coli* expression with SPR for experimental validation (taking approximately 6 weeks and 2 weeks post-oligonucleotide order, respectively), and OrthoRep affinity maturation.

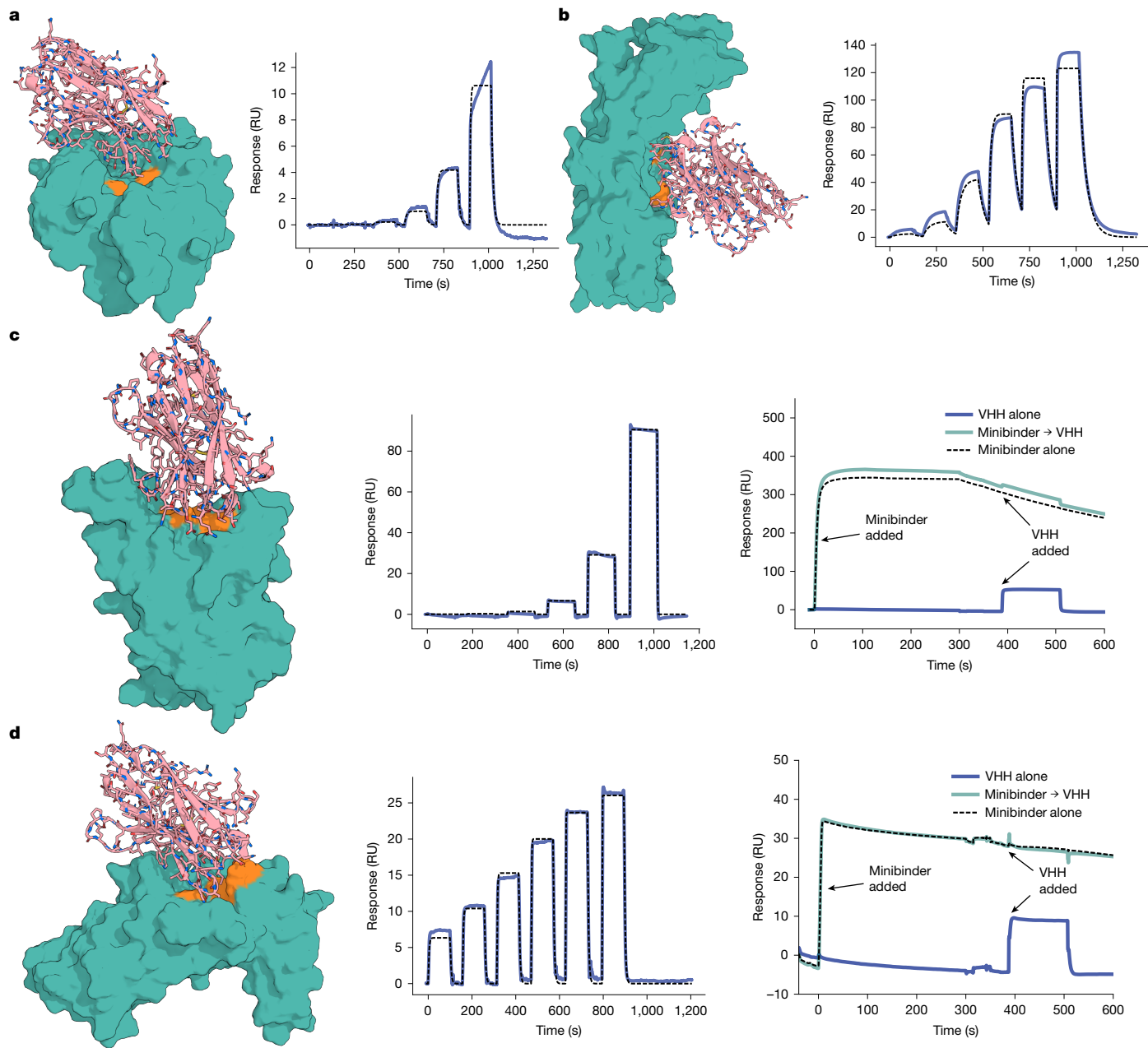


**Fig. 2 | Biochemical characterization of designed VHHS.** **a,b**, Nine thousand designed VHHS were screened against RSV site III (**a**; VHH\_RSV\_01) and influenza haemagglutinin (**b**; VHH\_Flu\_01) with yeast surface display, before soluble expression of the top hits in *E. coli*. SPR demonstrated that the highest affinity VHHS to RSV site III and influenza haemagglutinin bound their respective targets with 1.4  $\mu$ M and 78 nM, respectively. **c**, Nine thousand VHH designs were tested against the SARS-CoV-2 RBD, and after soluble expression, SPR confirmed an affinity of 5.5  $\mu$ M to the target for design VHH\_RBD\_D4 (left). Binding was to the expected epitope, confirmed by competition with a

structurally confirmed de novo binder (AHB2 (PDB ID 7UHB), right). **d**, Ninety-five VHH designs were tested against *C. difficile* TcdB. The highest affinity VHH, VHH\_TcdB\_H2, bound with 262 nM affinity (left), and also competed with a structurally confirmed de novo binder (FZD48, PDB ID 9CM5 (ref. 29)) to the same epitope (right). See also Extended Data Fig. 4a–c for quantification of the competition shown in panels **c,d**. For all panels, the measured binding response is indicated in a solid blue line, and the global fit using a 1:1 binding interaction model is indicated with a black dashed line.

to a range of disease-relevant targets: *C. difficile* TcdB, influenza H1 haemagglutinin, respiratory syncytial virus (RSV) sites I and III, SARS-CoV-2 receptor-binding domain (RBD) and IL-7R $\alpha$ . Computationally filtered designs were screened either at high throughput by yeast surface display (9,000 designs per target; RSV sites I and III, RBD and influenza haemagglutinin) or at lower throughput with *Escherichia coli* expression and single-concentration surface plasmon resonance (SPR; 95 designs per target; TcdB, IL-7R $\alpha$  and influenza haemagglutinin; the latter was screened using both methods).

The highest affinity binders to RSV site III, influenza haemagglutinin, RBD and TcdB are shown in Fig. 2a–c,e, respectively (see also Supplementary Fig. 2 for all the SPR traces of confirmed VHH binders identified in this study and Supplementary Methods Table 6 for success rates against each target, which range from 0% to 2%). The CDR loops are distinct from VHHS observed in nature, indicating substantial generalization beyond the training dataset (Extended Data Fig. 1). Of the haemagglutinin binders tested against the insect-cell-produced haemagglutinin monomer, the highest affinity binder had a dissociation

constant ( $K_d$ ) of 78 nM (Fig. 2b), with other binders having affinities of 546 nM, 698 nM and 790 nM. For TcdB, the target epitope was the Frizzled interface, for which there are no antibodies or VHHS targeting this site in the PDB. For the best-designed VHH from both RBD ( $K_d = 5.5 \mu\text{M}$ ; Fig. 2c) and TcdB ( $K_d = 260 \text{ nM}$ ; Fig. 2d), binding was confirmed to be to the desired epitope: binding was completely abolished upon addition of a previously designed, structurally characterized de novo binder to that epitope (AHB2 (PDB ID 7UHB<sup>28</sup>) for RBD and FZD48 (PDB ID 9CM5 (ref. 29)) for TcdB; Fig. 2c,d and Extended Data Fig. 4a–c). This TcdB VHH also neutralized TcdB toxicity in *CSPG4*-knockout cells (an alternative TcdB receptor) with a half-maximal effective concentration (EC<sub>50</sub>) of 460 nM (Extended Data Fig. 4d,e). For TcdB, the interactions were specific, with no binding observed to the highly related (70% sequence homology) *Paeniclostridium sordellii* lethal toxin L (TcsL; Extended Data Fig. 4b). These data demonstrate the ability of RFdiffusion to design VHHS that make specific interactions with the target epitope.

### Cryo-EM of a VHH-binding influenza haemagglutinin

We sought to evaluate design accuracy by cryo-electron microscopy (cryo-EM) structure determination of the designed anti-haemagglutinin VHHS in complex with natively glycosylated, trimeric influenza haemagglutinin glycoprotein (strain A/USA/Iowa/1943 H1N1; Supplementary Fig. 4), which retains the conserved stem epitope used during computational VHH design and upstream biochemical screening. Cryo-EM data processing revealed that one VHH design effectively bound to the fully glycosylated haemagglutinin trimer (out of the four tested), denoted hereafter as VHH\_flu\_01 (Fig. 3 and Extended Data Fig. 5). Two-dimensional classification of all particles in the dataset (Fig. 3a) and the determined 3.0 Å structure of the complex (Fig. 3b and Supplementary Methods Table 10) identified approximately 66% of haemagglutinin particles bound to a maximum of two VHHS per trimer (Fig. 3a–h). This partial occupancy is probably attributable to the N296 glycan, which, in unbound subunits, partially occludes the target epitope but reorients when bound to VHH\_flu\_01 (see Fig. 3h).

The structure of influenza haemagglutinin bound to two copies of VHH\_flu\_01 (Fig. 3b,c and Extended Data Fig. 5) reveals a VHH approach angle that closely matches the predicted model (Fig. 3f) and a VHH backbone that is very close to the RFdiffusion design, with a calculated root mean square deviation (RMSD) of 1.45 Å (Fig. 3g). The CDR3 structure is also very similar between the cryo-EM structure and the computational model (RMSD = 0.8 Å; Fig. 3d), with residues V100, V101, S103 and F108 in the de novo-designed CDR3 loop interacting with the influenza haemagglutinin stem epitope in the cryo-EM structure, as designed by RFdiffusion and re-predicted with RF2 (Fig. 3e). The design is highly dissimilar from the closest antibody–VHH binding to this epitope in the PDB (Extended Data Fig. 1f,g and Supplementary Fig. 5). Together, these results demonstrate the VHH design with atomic-level precision.

### Cryo-EM of VHHS to TcdB and SARS-CoV-2

To improve the binding affinity of de novo-designed VHHS, we utilized the orthogonal error-prone DNA replication system, OrthoRep, for continuous hypermutation of target genes *in vivo*<sup>30,31</sup>. OrthoRep has been shown to drive the rapid affinity maturation of yeast surface-displayed antibodies. We used this capability to affinity-mature VHHS targeting TcdB, influenza H1 haemagglutinin and the SARS-CoV-2 RBD. Affinity-matured VHHS acquired several mutations relative to the parent designs and improved binding affinities by approximately two orders of magnitude (Supplementary Fig. 3), making them suitable candidates for downstream cryo-EM structural characterization.

For TcdB, our design campaign targeted the Frizzled-binding epitope located on the RBD. TcdB consists of four functional domains including a central delivery and RBD (DRBD) where the VHHS were designed

to bind. Cryo-EM characterization of the original parent design, VHH\_TcdB\_H2, confirmed that the VHH engages the target Frizzled DRBD epitope (Supplementary Fig. 7). Analysis via two-dimensional and three-dimensional classification revealed a mix of bound and unbound TcdB particles (Fig. 3i and Supplementary Figs. 6 and 7). Extensive three-dimensional classification and local refinement identified multiple structural states of TcdB within the dataset, including an extended bound state (Extended Data Fig. 6 and Supplementary Fig. 8). Three-dimensional refinement of the bound VHH in the extended TcdB state yielded a modest 4.6 Å map, into which the design model was confidently rigid-body docked, showing high agreement with the intended design structure (Fig. 3i–k). To evaluate whether the improved affinity achieved through OrthoRep preserved the original binding mode of the parent design, we performed additional cryo-EM analysis on the affinity-matured VHH, VHH\_TcdB\_H2\_ortho. These experiments revealed a high proportion of TcdB particles now bound by the VHH, consistent with its enhanced affinity (Fig. 3l–n and Supplementary Fig. 3b). Using a similar processing pipeline as for the parent VHH–TcdB complex, we resolved the affinity-matured VHH–TcdB complex to a modest 5.7 Å resolution, enabling us to confidently dock the designed VHH into the cryo-EM density with close agreement. This confirmed that the VHH maintained targeting to the correct epitope and retained its original binding pose after OrthoRep-mediated affinity maturation (Fig. 3l–n and Extended Data Fig. 6). These results underscore the capability of RFdiffusion to design accurate de novo VHHS that are capable of targeting previously unexplored epitopes and are amenable to downstream affinity maturation.

We next used cryo-EM to characterize an affinity-matured VHH (VHH\_RBD\_D4\_ortho19) targeting the SARS-CoV-2 spike RBD, where competition experiments indicated that the parental VHH bound the intended epitope (Fig. 2c, Extended Data Fig. 4c and Supplementary Figs. 3b and 9). The RBD transitions between ‘up’ and ‘down’ conformations, with the ‘up’ state enabling receptor binding and viral entry<sup>32</sup>. Cryo-EM two-dimensional class averages and three-dimensional classification reconstructions of the VHH-bound complex revealed a mixture of RBD conformations (1–2 ‘up’), with VHH density observed exclusively in the up state. This is consistent with its design, as the target epitope is occluded in the down conformation (Supplementary Fig. 9a,b). Global refinement with an average estimated resolution of 3.9 Å provided well-defined density for the lower portion of the spike protein (local resolution of approximately 2.5 Å), but the relative flexibility of the RBD resulted in substantial signal averaging, causing density loss at higher contour levels, which precluded assessment of VHH design accuracy (Supplementary Fig. 9c–e). Symmetry expansion and local refinement helped improve the resolution of the RBD–VHH interface, confirming the intended VHH fold and accurate epitope targeting following rigid-body docking of the design model into the density map (Supplementary Fig. 9f,g), in agreement with our biochemical competition data (Fig. 2c). However, although the VHH bound the correct RBD epitope, its binding mode deviated notably from the design model, instead adopting a predominantly framework-mediated interaction that more closely matched retrospective AlphaFold3 predictions (Supplementary Fig. 9g,h). Owing to the deviation between the designed dock and the experimentally determined dock, we classified this as a design failure.

### Design of scFvs with six designed CDRs

Given the success of RFdiffusion at designing VHHS with three de novo CDRs, we next tested its ability to design both heavy and light chains in scFv format. RFdiffusion was used to generate scFvs targeting specific epitope sites, following a strategy similar to the VHH design approach. However, unlike VHHS, where only three CDRs were built de novo, scFv design involved constructing all six CDRs on both the heavy and the light chains in addition to the docking mode.

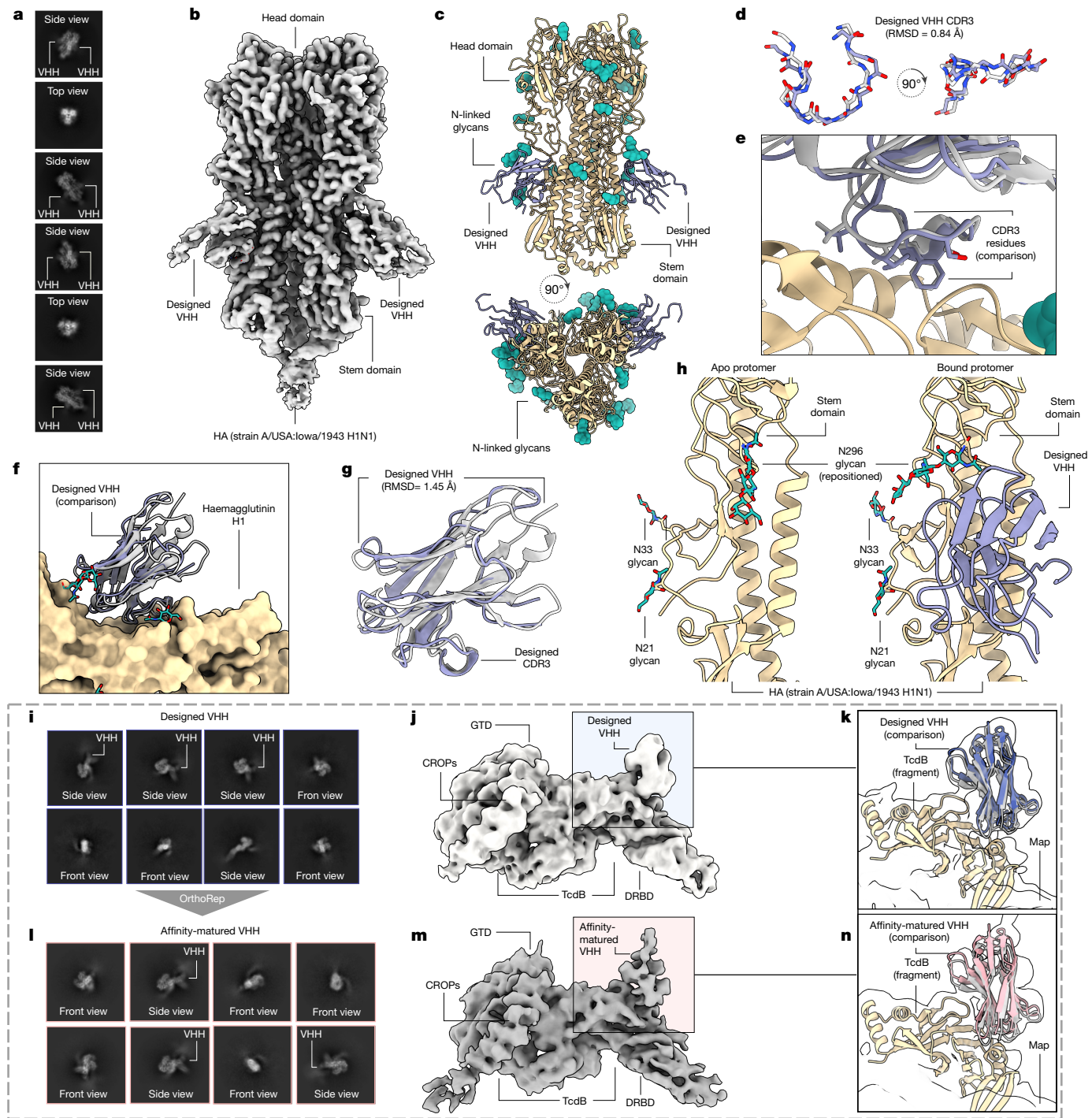


**Fig. 3 | Cryo-EM structural characterization of de novo-designed VHH binding to influenza haemagglutinin and TcdB.** **a**, Labelled cryo-EM two-dimensional class averages of designed VHH\_fiu\_01 bound to influenza haemagglutinin (HA) strain A/USA:Iowa/1943 H1N1. **b**, The 3.0 Å cryo-EM three-dimensional reconstruction shows VHH\_fiu\_01 bound to H1 along the stem in two protomers. **c**, Cryo-EM structure of VHH\_fiu\_01 bound to influenza haemagglutinin. **d**, Superposition of the designed VHH CDR3 structure with the cryo-EM structure. **e**, Comparison of predicted CDR3 rotamers compared with the built 3.0 Å cryo-EM structure. **f,g**, The cryo-EM structure closely matches the design. **h**, Examination of apo haemagglutinin protomers juxtaposed with those bound to the designed VHH shows repositioning of glycan N296 to allow for binding of the designed VHH to the stem. **i**, Labelled cryo-EM two-dimensional class averages of the designed VHH, VHH\_TcdB\_H2\_bound to full-length TcdB. **j**, The 4.6 Å cryo-EM three-dimensional reconstruction of the complex shows VHH\_TcdB\_H2\_bound to the target epitope as predicted. CROPs, combined repetitive oligopeptides; GTD, glucosyltransferase domain. **k**, Owing to the

modest resolution, a fragment of TcdB was first docked into the cryo-EM density map, and the full design model—including both the TcdB fragment and the designed VHH—was then aligned to the pre-fitted TcdB fragment. The predicted design closely matches the experimentally determined complex in structure, epitope targeting and overall conformation. **l**, Labelled cryo-EM two-dimensional class averages of the designed VHH, VHH\_TcdB\_H2\_ortho, bound to full-length TcdB. **m**, The 5.7 Å cryo-EM three-dimensional reconstruction of the complex shows that VHH\_TcdB\_H2\_ortho bound the target epitope as predicted. **n**, A TcdB fragment was docked into the cryo-EM map, followed by alignment of the full model including the OrthoRep-matured VHH. The resulting structure shows no detectable change in binding orientation or docking angle compared with the original design, indicating that OrthoRep maturation preserved the predicted mode of epitope engagement. In all panels: yellow indicates haemagglutinin; grey denotes the computational design prediction; pink or navy shows VHH (cryo-EM); and teal indicates glycan.

The gene synthesis problem is more formidable for scFvs than for VHVs as they are too long to be simply assembled from pairs of conventional oligonucleotides synthesized on oligonucleotide arrays, and are challenging to uniquely pair due to high sequence homology between scFvs. We developed stepwise assembly protocols that enable the construction of libraries with heavy and light chains either specifically paired as in the design models (Supplementary Figs. 10 and 11) or combinatorially mixed within subsets of designs specifically with similar target-binding modes (Supplementary Fig. 12). The latter approach helps to overcome the greater challenge of accurate design of six CDRs de novo, which increases the possibilities for error compared with the VHH problem as only one suboptimal CDR can compromise binding. We found that given sets of nearly superimposable designs targeting the same site with the same binding mode, new scFvs generated by combining pairs of heavy and light chains from different designs were confidently predicted to bind to the target site in the designed binding mode at similar frequencies as compared to the original designs (Extended Data Fig. 7a). By contrast, random, structure-agnostic pairing rarely led to predicted binders (Extended Data Fig. 7a). Hence, by mixing CDRs from different designs that bind in the same orientation, we can effectively overcome failures due to single imperfectly designed CDRs, thereby offering a combinatorial solution to a combinatorially more complex problem (two-chain scFv design versus one-chain VHH design). This strategy highlights a key advantage of structure-based design: ‘intelligent’ pairing of heavy and light chains is possible with a structural model of every antibody, and allows de novo-designed antibody libraries to reach scales attainable by traditional library assembly methods, despite current limits in gene synthesis.

We succeeded in identifying epitope-specific scFvs from the heavy-light combinatorial libraries (of a theoretical complexity of approximately 10 million; Extended Data Figs. 7b,c and 8a–c) but not the fixed pairing libraries (Supplementary Fig. 13). Following expression and purification, SPR analysis of six distinct scFvs originating from two unique docks targeting the Frizzled epitope of TcdB revealed a range of affinities (Fig. 4d–h): the highest affinity binder, scFv6, had a  $K_d$  of 72 nM (Fig. 4g). Conversion of the scFv to a full length IgG1 generated antibodies that bind with comparable (68 nM) affinity, demonstrating that our design method can be used to generate full-length antibodies (Fig. 4i). There are no antibodies binding to this epitope in the PDB, hence, this success cannot be attributed to memorization. Subsequent prediction of the structure of the scFv with AlphaFold3 showed a binding mode identical to that of the two nearly superimposable parent designs that contributed the light and heavy chains (Supplementary Fig. 16c,d). Competition with a known receptor, Frizzled-7, to this epitope confirmed that binding of scFv5 was on target (Fig. 4j). By contrast, no competition was seen in the presence of CSPG4, an alternative receptor that interacts with an epitope at the toxin core. Thus, scFvs targeting user-specified epitopes can be identified from structure-aware designed combinatorial libraries.

We next targeted a clinically relevant epitope: the QYNPIRTTF peptide derived from the *PHOX2B* neuroblastoma-dependency gene and master transcriptional regulator in complex with the major histocompatibility complex (MHC) allotype HLA-C\*07:02 (we refer to this peptide below simply as PHOX2B). The PHOX2B peptide was originally discovered by immunopeptidomics of neuroblastoma patient-derived samples, and has been targeted with peptide-centric chimeric antigen receptors (PC-CARs) for treating high-risk neuroblastoma<sup>33</sup>. However, the PC-CARs identified previously are restricted to recognizing PHOX2B presented on HLAs of the A9 serological group, excluding the common allotype HLA-C\*07:02 (ref. 34). Targeting the PHOX2B–HLA-C\*07:02 complex could meaningfully increase the addressable patient population for these immunotherapies, and has been the focus of ongoing therapeutics development. Recently, computationally designed (non-antibody) binders for PHOX2B–HLA-C\*07:02 have

been developed, using the TRACeR-I system<sup>35</sup>, whereas high-affinity TCRs have been identified for targeting peptides on the common HLA-C\*08:02/HLA-C\*05:01 allotypes<sup>36</sup>. A benefit of structure-based design is the ability to target specific peptide residues to achieve binding specificity (rather than binding only to the MHC), and we therefore used RFdiffusion to target the R6 residue, which is known to be important for binding in the PC-CAR<sup>34</sup>. Given the low stability of the PHOX2B–HLA-C\*07:02 complex ( $T_m$  of 44.2 °C)<sup>34</sup>, we leveraged a disulfide-stabilized approach to prepare a stabilized form of the pHLA target<sup>37</sup>. Using the combinatorial assembly approach described above, we identified modest-affinity (400 nM as measured by SPR and 1 μM as measured by isothermal titration calorimetry (ITC); Fig. 4k,l and Extended Data Fig. 8e–g) scFv binders to PHOX2B–HLA-C\*07:02. Binding was specific to the peptide, with no detectable binding to the R6A point mutant PHOX2B peptide (PHOX2B(R6A)–HLA-C\*07:02; Fig. 4l). Attempts were made to incorporate scFv binders into a 4-1BB-CAR, but T cell cytotoxicity assays demonstrated no detectable killing of a range of neuroblastoma cell lines (Supplementary Fig. 14), probably because of the modest binding affinity and/or low levels of antigen density expressed on the tumour cells. Although there is still considerable room for improvement in affinity, this demonstrates the ability of structure-based antibody design, paired with appropriate library assembly methods, to design specific binders to challenging and clinically important target epitopes.

## Atomically accurate scFv design to TcdB

To evaluate the accuracy of de novo scFv design, we determined the cryo-EM structures of two combinatorially assembled scFvs, scFv5 and scFv6, both targeting the Frizzled epitope of TcdB. Cryo-EM analysis confirmed that both scFvs bound the Frizzled epitope as designed (Fig. 5 and Extended Data Fig. 9). High-resolution two-dimensional class averages of scFv6 revealed clear density for both TcdB and the bound scFv, further supported by a 3.6 Å three-dimensional reconstruction (Fig. 5a,b and Extended Data Fig. 9). The resolved structure showed that scFv6 engaged the Frizzled epitope along its DRBD domain with the predicted binding orientation (Fig. 5d and Supplementary Methods Table 10). Superposition of the cryo-EM structure with the design model demonstrated remarkable agreement, with both heavy and light chains interacting with the epitope as intended (Fig. 5c and Supplementary Fig. 16a,b). The overall fold closely matched the design, a composite model of the two chains originating from distinct but structurally similar designs (RMSD = 0.9 Å), and each of the six CDRs exhibited near-atomic precision (backbone RMSDs: CDRH1 = 0.4 Å, CDRH2 = 0.3 Å, CDRH3 = 0.7 Å, CDRL1 = 0.2 Å, CDRL2 = 1.1 Å and CDRL3 = 0.2 Å; Fig. 5e,f). This agreement extended to the rotameric conformations of CDR side chains and their interactions with the Frizzled epitope, underscoring the accuracy of RFdiffusion in designing de novo scFv–target interactions (Fig. 5g).

scFv5 was designed to bind to the same epitope but with a distinct approach angle relative to scFv6 (Fig. 4b,c). A 6.1 Å cryo-EM reconstruction confirmed scFv5 binding to the TcdB Frizzled epitope, with two-dimensional class averages showing clear density for the complex (Fig. 5h and Supplementary Fig. 15). Rigid-body docking of the design model into the cryo-EM density revealed close agreement between the predicted-binding and experimentally determined-binding modes (Fig. 5i,j).

## Improved oracles increase success rate

Although our results demonstrate that the de novo design of antibodies is possible, the experimental success rates remain low. A key contributor to previous successes in de novo binder design was improved filters (primarily AlphaFold2 (ref. 19), which enriched for experimental success in the subset of designs that are tested experimentally<sup>2,22</sup>). At the outset

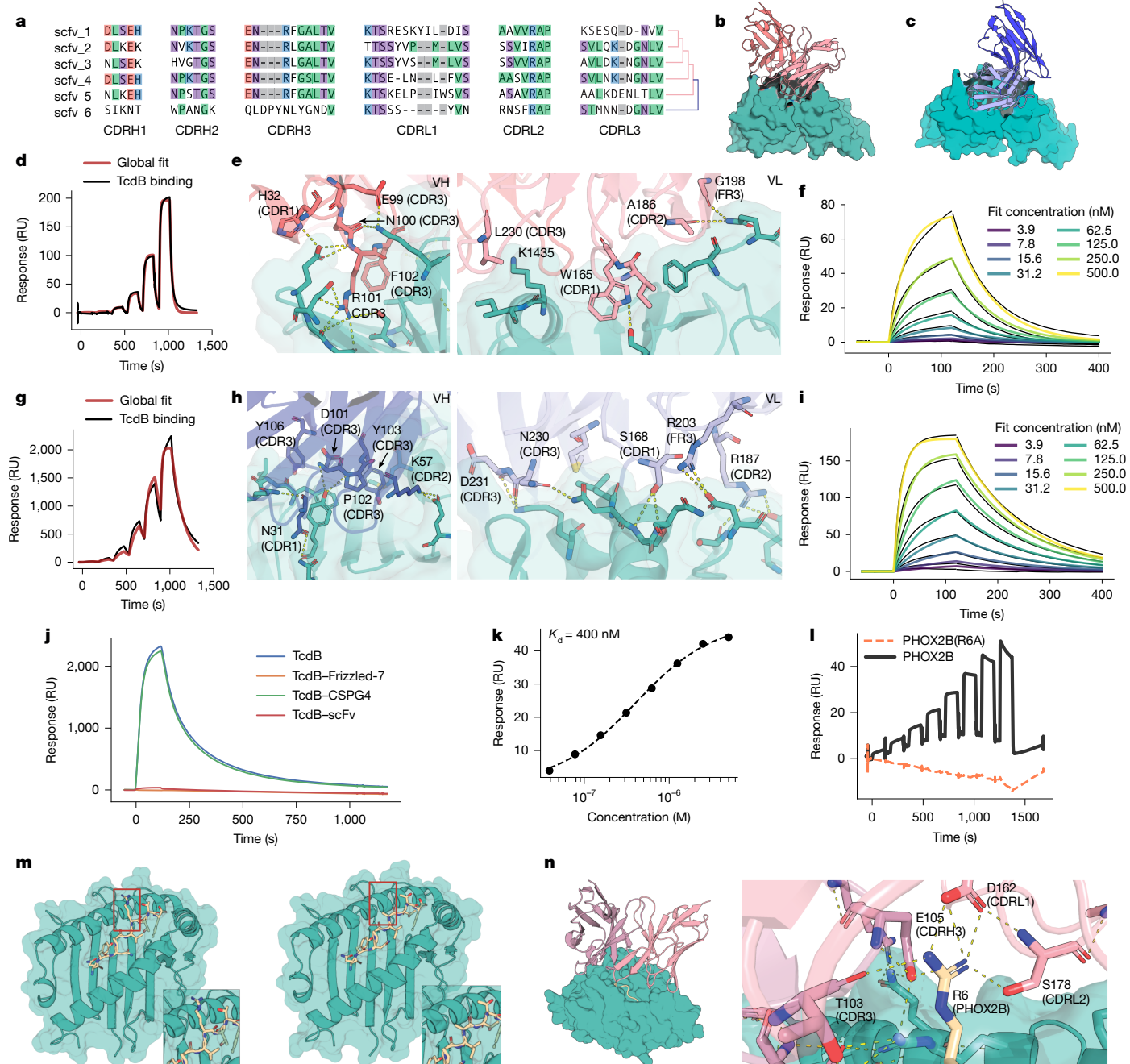


**Fig. 4 | Biochemical characterization of combinatorially assembled scFvs with six designed CDRs.** **a**, Multiple sequence alignment of six scFvs that bind to TcdB. scFvs 1–5 originate from the same structural cluster, whereas scFv6 originates from a distinct cluster. **b,c**, AlphaFold3 predictions of scFv5 (**b**) and scFv6 (**c**) in complex with TcdB. scFv5 and scFv6 are predicted to bind to a similar but not identical epitope. The predicted orientation of scFv6 relative to TcdB is rotated compared with scFv5. **d**, Affinity of scFv5 to TcdB was 460 nM by SPR. **e**, Computational prediction of the scFv5–TcdB interface for VH (variable heavy-chain fragment; left) and VL (variable light-chain fragment; right). **f**, scFv5, when expressed as a full-length IgG1, shows a binding affinity of 380 nM to TcdB by SPR. **g**, Affinity of scFv6 to TcdB was 72 nM by SPR. **h**, Computational prediction of the scFv6–TcdB interface for VH (left) and VL (right). **i**, scFv6, when expressed as a full-length IgG1, shows a binding affinity of 68 nM to TcdB by SPR. **j**, scFv5 competes with Frizzled-7 and does not compete with CSPG4, indicating

on-target binding. scFv5 was conjugated to a CM5 chip and TcdB RBD was flowed over at 50 nM either alone or mixed with 1 μM of Frizzled-7, CSPG4 or scFv5. **k,l**, SPR comparative analysis of B1.2.1 binding to C\*07:02-PHOX2B versus C\*07:02-PHOX2B(R6A). scFv was immobilized and then on-target and off-target binding was measured across an eight-step, twofold titration with an upper concentration of 5 μM. Steady-state kinetic analysis (**k**) and raw SPR trace (**l**) of on-target and off-target binding indicate specific binding to the intended target. **m**, AlphaFold3 predictions of HLA-C\*07:02 with peptide PHOX2B (left) and PHOX2B(R6A) (right). R6 of PHOX2B is predicted to be solvent exposed. **n**, AlphaFold3 prediction of scFv B1.2.1 in complex with C\*07:02-PHOX2B (left). Predicted polar contacts with R6 of the PHOX2B peptide (right), mediated by CDRH3, CDRL1 and CDRL2, are also shown. Figure was created using BioRender (<http://biorender.com>).

of this study, we sought to build such a filter by fine-tuning RoseTTAFold2 (Extended Data Figs. 2 and 3), but the filtering power of this model is limited (at least with the settings used; providing 100% of interface

'hotspots'). This probably accounts for the low experimental success rates and the inaccurate SARS-CoV-2 design, where the overall fold and epitope targeting were correct, but the binding orientation was not.

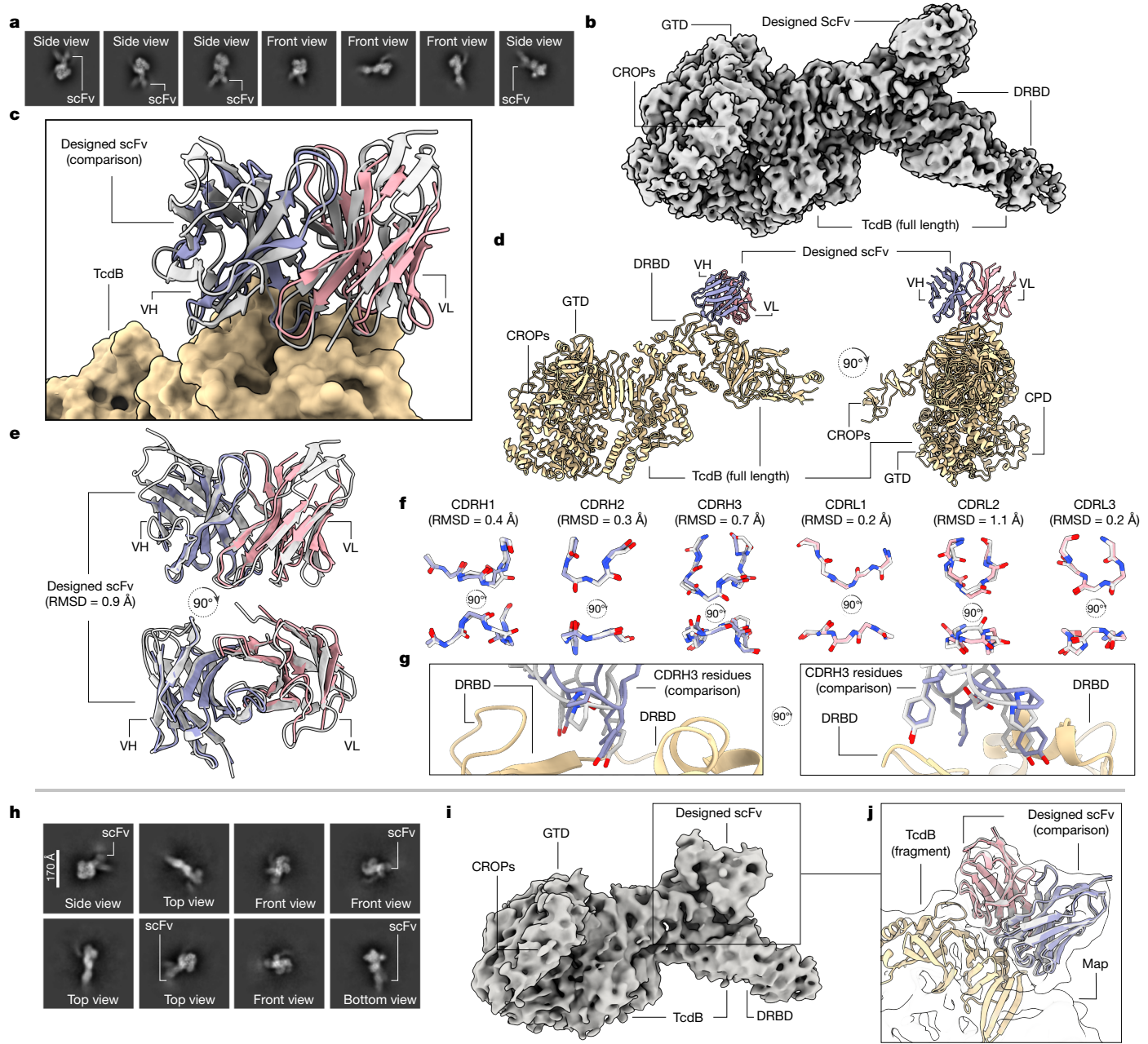


**Fig. 5 | Cryo-EM structural characterization of two TcdB-binding scFvs.**

**a**, Labelled cryo-EM two-dimensional class averages of a designed scFv, scFv6, bound to TcdB. **b**, A 3.6 Å cryo-EM three-dimensional reconstruction of the complex shows scFv6 bound to TcdB along the Frizzled epitope. **c**, The cryo-EM structure of scFv6 in complex with TcdB closely matches the design model. **d**, Cryo-EM structure of scFv6 bound to TcdB. **e**, Cryo-EM reveals the accurate design of scFv6 using RFdiffusion. **f**, Superposition of each of the six designed scFv6 CDR loop predicted structures as compared with the built cryo-EM structure. **g**, Comparison of predicted CDRH3 rotamers compared with the built 3.6 Å cryo-EM structure. **h**, Labelled cryo-EM two-dimensional class averages of the designed scFv, scFv5, bound to full-length TcdB. **i**, A 6.1 Å

cryo-EM three-dimensional reconstruction of the complex shows the scFv5 bound to the target epitope as predicted. **j**, Owing to the modest resolution, a fragment of TcdB was first docked into the cryo-EM density map, and the full design model—including both the TcdB fragment and the designed scFv—was then aligned to the pre-fitted TcdB fragment. This approach demonstrates that the predicted design closely matches the experimentally determined complex in structure, epitope targeting and overall conformation. In models, yellow denotes TcdB; navy indicates the variable heavy-chain fragment (cryo-EM); pink shows the variable light-chain fragment (cryo-EM); and grey denotes the computational design prediction.

Subsequent to the design work in this study, AlphaFold3 (ref. 24) was released and has improved antibody structure prediction accuracy<sup>24,38</sup>, both with<sup>24,38</sup> and without<sup>38</sup> antigen present. Retrospectively, we can assess how filtering with AlphaFold3 would have improved experimental success rates. First, AlphaFold3 accurately predicts the experimentally validated structure of the inaccurately designed SARS-CoV-2 VHH (Supplementary Fig. 9). Had AlphaFold3 been used

as an initial filter, this design would have been rejected due to the discrepancy between the predicted and intended structures, thereby preventing its experimental testing. Second, we predicted the structures of the SARS-CoV-2, influenza haemagglutinin, TcdB and IL-7R $\alpha$  VHH designs using AlphaFold3 with a multiple sequence alignment (MSA) and templates for the target and only a template for the VHH (as CDRs are de novo, we reasoned the MSA would be of limited utility).

# Article

We analysed the predictions for libraries with at least one structurally validated VHH (TcdB, influenza haemagglutinin and SARS-CoV-2). These results are dominated by anti-haemagglutinin VHHs as the majority of successful binders came from this library. We found that the AlphaFold3 interface predicted template modelling (ipTM) score, a measure of model confidence over the interface, is predictive of binding success (area under the curve = 0.86; Extended Data Fig. 10a,b). Overall, only 9% of our ordered VHH designs have an ipTM > 0.6, suggesting that success rate will be improved by incorporation of an ipTM filter. We ran a similar analysis for the combinatorially assembled scFv libraries; we predicted the structures of the parental scFv designs (before combinatorial assembly) and the experimentally confirmed scFv designs (combinatorially assembled) using AlphaFold3 with an MSA for the target sequence and templates for the target as well as the heavy and light chains, taking the maximum ipTM score over 10 seeds. We found that successful designs cluster to higher AlphaFold3 ipTM scores than the parental designs (Extended Data Fig. 10c). Only 4% of the initial design library has ipTM > 0.85, whereas 5 out of the 6 experimentally confirmed designs pass this threshold, again suggesting that filtering by AlphaFold3 ipTM should increase success rates (Extended Data Fig. 10d).

## Discussion

Our results demonstrate that de novo design of antibody domains targeting specific epitopes on a target is possible. The cryo-EM structural data for the designed VHHs to influenza haemagglutinin and TcdB reveals very close agreement to the computational design models, showing that our approach can design VHH complexes with atomic accuracy—including the highly variable H3 loop and the overall binding orientation—that are highly dissimilar from any known structures in the PDB. Moreover, cryo-EM structural data of designed scFvs bound to TcdB demonstrate the ability of RFdiffusion to design two-chain scFvs accurately. To our knowledge, these are the first structurally validated cases of de novo-designed antibodies.

Our computational method synergizes with experimental screening approaches developed for retrieving antibodies from large random libraries in several ways. First, yeast display selection methods widely used for antibody library screening enable the retrieval of the highest affinity binders among large sets of designs, which is currently necessary due to the quite low design success rate. Second, screening combinatorial libraries that mix heavy and light chains from designs with similar binding modes allows for the identification of scFvs composed of structurally compatible chains targeting specific epitopes, as demonstrated here for TcdB and PHOX2B-peptide MHC. Third, affinity maturation using OrthoRep<sup>3</sup> improves the measured affinity of initial VHH designs down to the single-digit nanomolar or subnanomolar range, while preserving the original designed-binding mode. From a practical standpoint, the key advance of this work is not the ability to generate VHHs and scFvs against a target—something often achievable through purely experimental methods—but rather the ability to accurately target specific binding epitopes. The epitope specificity is critical for therapeutic applications such as antagonists that block receptor–ligand interactions, antibodies that avoid competing with endogenous molecules, modulators that induce conformational changes to trigger signalling, or antibodies targeting conserved or evolutionarily restricted viral epitopes.

There remains considerable room for improvement. For the backbone design step, incorporating recent architectural improvements<sup>39</sup> and new advances in generative modelling<sup>40–42</sup> may yield design models with higher designability and diversity. RoseTTAFold2 and RFdiffusion have also recently been extended to model all biomolecules (rather than just proteins)<sup>43</sup>, and incorporating this capability into the antibody design RFdiffusion variant should permit the accurate design of antibodies to epitopes containing non-protein

atoms, such as glycans. ProteinMPNN was not modified in this current work, but designing sequences that more closely match human CDR sequences would be expected to reduce the potential immunogenicity of designed antibodies<sup>44,45</sup>. Indeed, designed sequences are currently somewhat less human (as assessed by an OASis score<sup>46</sup>) than therapeutic antibody CDRs (Supplementary Fig. 1d). Further improvements in antibody structure prediction methods should allow faster optimization of upstream design methods and improve experimental success rates.

Ultimately, computational de novo design of antibodies using our RFdiffusion and related approaches<sup>47</sup> could revolutionize antibody discovery and development. As the method improves and success rates increase, it has the potential to be faster and more cost-effective than immunizing animals or screening random libraries. A structure-based approach to antibody design should also aid the optimization of key pharmaceutical properties, such as aggregation, solubility and expression levels (all major challenges in antibody development) in a structure-informed manner. Together, we expect that computational design of antibodies will increase the number of tractable clinical targets and diseases accessible to antibody therapeutics.

## Online content

Any methods, additional references, Nature Portfolio reporting summaries, source data, extended data, supplementary information, acknowledgements, peer review information; details of author contributions and competing interests; and statements of data and code availability are available at <https://doi.org/10.1038/s41586-025-09721-5>.

1. Wilson, P. C. & Andrews, S. F. Tools to therapeutically harness the human antibody response. *Nat. Rev. Immunol.* **12**, 709–719 (2012).
2. Watson, J. L. et al. De novo design of protein structure and function with RFdiffusion. *Nature* **620**, 1089–1100 (2023).
3. Paulk, A. M., Williams, R. L. & Liu, C. C. Rapidly inducible yeast surface display for antibody evolution with OrthoRep. *ACS Synth. Biol.* **13**, 2629–2634 (2024).
4. Lyu, X. et al. The global landscape of approved antibody therapies. *Antib. Ther.* **5**, 233–257 (2022).
5. Sormanni, P., Aprile, F. A. & Vendruscolo, M. Rational design of antibodies targeting specific epitopes within intrinsically disordered proteins. *Proc. Natl Acad. Sci. USA* **112**, 9902–9907 (2015).
6. Liu, X. et al. Computational design of an epitope-specific Keap1 binding antibody using hotspot residues grafting and CDR loop swapping. *Sci. Rep.* **7**, 41306 (2017).
7. Leaver-Fay, A. et al. ROSETTA3: an object-oriented software suite for the simulation and design of macromolecules. *Methods Enzymol.* **487**, 545–574 (2011).
8. Xie, X., Valiente, P. A., Lee, J. S., Kim, J. & Kim, P. M. Antibody-SGM, a score-based generative model for antibody heavy-chain design. *J. Chem. Inf. Model.* **64**, 6745–6757 (2024).
9. Eguchi, R. R. et al. Deep generative design of epitope-specific binding proteins by latent conformation optimization. Preprint at *bioRxiv* <https://doi.org/10.1101/2022.12.22.521698> (2022).
10. Shafehazzadeh, A. et al. Unlocking de novo antibody design with generative artificial intelligence. Preprint at *bioRxiv* <https://doi.org/10.1101/2023.01.08.523187> (2023).
11. Porebski, B. T. et al. Rapid discovery of high-affinity antibodies via massively parallel sequencing, ribosome display and affinity screening. *Nat. Biomed. Eng.* **8**, 214–232 (2024).
12. Agarwal, A. A. et al. AlphaBind, a domain-specific model to predict and optimize antibody–antigen binding affinity. *mAbs* **17**, 2534626 (2025).
13. Vázquez Torres, S. et al. De novo design of high-affinity binders of bioactive helical peptides. *Nature* **626**, 435–442 (2024).
14. Sappington, I. et al. Improved protein binder design using beta-pairing targeted RFdiffusion. Preprint at *bioRxiv* <https://doi.org/10.1101/2024.10.11.617496> (2024).
15. Cao, L. et al. Design of protein-binding proteins from the target structure alone. *Nature* **605**, 551–560 (2022).
16. Gainza, P. et al. De novo design of protein interactions with learned surface fingerprints. *Nature* **617**, 176–184 (2023).
17. Pacesa, M. et al. One-shot design of functional protein binders with BindCraft. *Nature* **646**, 483–492 (2025).
18. Cutting, D., Dreyer, F. A., Errington, D., Schneider, C. & Deane, C. M. De novo antibody design with SE(3) diffusion. Preprint at *arXiv* <https://doi.org/10.48550/arXiv.2405.07622> (2024).
19. Jumper, J. et al. Highly accurate protein structure prediction with AlphaFold. *Nature* **596**, 583–589 (2021).
20. Yang, J. et al. Improved protein structure prediction using predicted interresidue orientations. *Proc. Natl Acad. Sci. USA* **117**, 1496–1503 (2020).
21. Wang, J. et al. Scaffolding protein functional sites using deep learning. *Science* **377**, 387–394 (2022).
22. Bennett, N. et al. Improving de novo protein binder design with deep learning. *Nat. Commun.* **14**, 2625 (2023).

23. Yin, R. & Pierce, B. G. Evaluation of AlphaFold antibody–antigen modeling with implications for improving predictive accuracy. *Protein Sci.* **33**, e4865 (2024).
24. Abramson, J. et al. Accurate structure prediction of biomolecular interactions with AlphaFold 3. *Nature* **630**, 493–500 (2024).
25. Jin, B., Odongo, S., Radwanska, M. & Magez, S. Nanobodies: a review of generation, diagnostics and therapeutics. *Int. J. Mol. Sci.* **24**, 5994 (2023).
26. Mitchell, L. S. & Colwell, L. J. Analysis of nanobody paratopes reveals greater diversity than classical antibodies. *Protein Eng. Des. Sel.* **31**, 267–275 (2018).
27. Vincke, C. et al. General strategy to humanize a camelid single-domain antibody and identification of a universal humanized nanobody scaffold. *J. Biol. Chem.* **284**, 3273–3284 (2009).
28. Hunt, A. C. et al. Multivalent designed proteins neutralize SARS-CoV-2 variants of concern and confer protection against infection in mice. *Sci. Transl. Med.* **14**, eabm1252 (2022).
29. Ragotte, R. J. et al. De novo design of potent inhibitors of clostridial family toxins. *Proc. Natl Acad. Sci. USA* **122**, e2509329122 (2025).
30. Rix, G. et al. Continuous evolution of user-defined genes at 1 million times the genomic mutation rate. *Science* **386**, eadm9073 (2024).
31. Ravikumar, A., Arzumanyan, G. A., Obadi, M. K. A., Javanpour, A. A. & Liu, C. C. Scalable, continuous evolution of genes at mutation rates above genomic error thresholds. *Cell* **175**, 1946–1957.e13 (2018).
32. Walls, A. C. et al. Unexpected receptor functional mimicry elucidates activation of coronavirus fusion. *Cell* **176**, 1026–1039.e15 (2019).
33. Yarmarkovich, M. et al. Targeting of intracellular oncoproteins with peptide-centric CARs. *Nature* **623**, 820–827 (2023).
34. Sun, Y. et al. Structural principles of peptide-centric chimeric antigen receptor recognition guide therapeutic expansion. *Sci. Immunol.* **8**, eadj5792 (2023).
35. Du, H. et al. Targeting peptide antigens using a multiallelic MHC I-binding system. *Nat. Biotechnol.* <https://doi.org/10.1038/s41587-024-02505-8> (2024).
36. Sim, M. J. W. et al. High-affinity oligoclonal TCRs define effective adoptive T cell therapy targeting mutant KRAS-G12D. *Proc. Natl Acad. Sci. USA* **117**, 12826–12835 (2020).
37. Sun, Y. et al. Universal open MHC-I molecules for rapid peptide loading and enhanced complex stability across HLA allotypes. *Proc. Natl Acad. Sci. USA* **120**, e2304055120 (2023).
38. Hitawala, F. N. & Gray, J. J. What has AlphaFold3 learned about antibody and nanobody docking, and what remains unsolved? Preprint at *bioRxiv* <https://doi.org/10.1101/2024.09.21.614257> (2024).
39. Wang, C. et al. Proteus: pioneering protein structure generation for enhanced designability and efficiency. Preprint at *bioRxiv* <https://doi.org/10.1101/2024.02.10.579791> (2024).
40. Yim, J. et al. Fast protein backbone generation with SE(3) flow matching. Preprint at *arXiv* <https://doi.org/10.48550/arXiv.2310.05297> (2023).
41. Bose, J. et al. SE(3)-stochastic flow matching for protein backbone generation. In *Proc. 12th International Conference on Learning Representations (ICLR*, 2024).
42. Geffner, T. et al. Protein: scaling flow-based protein structure generative models. In *Proc. 13th International Conference on Learning Representations (ICLR*, 2025).
43. Krishna, R. et al. Generalized biomolecular modeling and design with RoseTTAFold All-Atom. *Science* <https://doi.org/10.1126/science.adl2528> (2024).
44. Gao, S. H., Huang, K., Tu, H. & Adler, A. S. Monoclonal antibody humanness score and its applications. *BMC Biotechnol.* **13**, 55 (2013).
45. Dreyer, F. A., Cutting, D., Schneider, C., Kenlay, H. & Deane, C. M. Inverse folding for antibody sequence design using deep learning. Preprint at <https://doi.org/10.48550/arXiv.2310.19513> (2023).
46. Prihoda, D. et al. BioPhi: a platform for antibody design, humanization, and humanness evaluation based on natural antibody repertoires and deep learning. *mAbs* **14**, 2020203 (2022).
47. Bio, N. & Biswas, S. De novo design of epitope-specific antibodies against soluble and multipass membrane proteins with high specificity, developability, and function. Preprint at *bioRxiv* <https://doi.org/10.1101/2025.01.21.633066> (2025).

**Publisher's note** Springer Nature remains neutral with regard to jurisdictional claims in published maps and institutional affiliations.



**Open Access** This article is licensed under a Creative Commons Attribution-NonCommercial-NoDerivatives 4.0 International License, which permits any non-commercial use, sharing, distribution and reproduction in any medium or format, as long as you give appropriate credit to the original author(s) and the source, provide a link to the Creative Commons licence, and indicate if you modified the licensed material. You do not have permission under this licence to share adapted material derived from this article or parts of it. The images or other third party material in this article are included in the article's Creative Commons licence, unless indicated otherwise in a credit line to the material. If material is not included in the article's Creative Commons licence and your intended use is not permitted by statutory regulation or exceeds the permitted use, you will need to obtain permission directly from the copyright holder. To view a copy of this licence, visit <http://creativecommons.org/licenses/by-nc-nd/4.0/>.

© The Author(s) 2025

# Article

## Reporting summary

Further information on research design is available in the Nature Portfolio Reporting Summary linked to this article.

## Data availability

The antibody training dataset is available on Zenodo<sup>48</sup> (<https://zenodo.org/records/15741710>). Cryo-EM maps and corresponding atomic models are located in the Electron Microscopy Data Bank (EMD-49373 and EMD-49405) and PDB (9NFU and 9NH7).

## Code availability

The codes for running the RFdiffusion antibody design, ProteinMPNN and fine-tuned RoseTTAFold have been released as a single repository on GitHub, free for academic, personal and commercial use (<https://github.com/RosettaCommons/RFantibody>).

48. Watson, J. L. Antibody training dataset for “Atomically accurate de novo design of antibodies with RFdiffusion” [data set]. Zenodo <https://doi.org/10.5281/zenodo.1574170> (2025).
49. Altschul, S. F. et al. Gapped BLAST and PSI-BLAST: a new generation of protein database search programs. *Nucleic Acids Res.* **25**, 3389–3402 (1997).
50. Dunbar, J. et al. SAbDab: the structural antibody database. *Nucleic Acids Res.* **42**, D1140–D1146 (2014).
51. Jäger, M., Gehrig, P. & Plückthun, A. The scFv fragment of the antibody hu4D5-8: evidence for early premature domain interaction in refolding. *J. Mol. Biol.* **305**, 1111–1129 (2001).
52. Kawai, S., Hashimoto, W. & Murata, K. Transformation of *Saccharomyces cerevisiae* and other fungi. *Bioeng. Bugs* **1**, 395–403 (2010).

**Acknowledgements** We thank P. Bradley for use of the TCR distillation dataset; M. Baek and F. DiMaio for training RoseTTAFold2; B. Coventry for the use of the de novo miniprotein binder dataset; J. Gershon for early contributions to this project; J.-P. Julien and I. Kucharska (The Hospital for Sick Children) for providing recombinant Frizzled-7 and CSPG4; N. Roullier for help with next-generation sequencing; A. Dosey for providing the haemagglutinin target protein; J. Dauparas, H. Kamisetty, A. Ebenezer, A. Motmaen and B. Lu for helpful discussions; I. Haydon for help with graphics; Twist Biosciences for access to their 400-bp oligo synthesis, which was invaluable for the high-throughput VH experiments; and L. Stewart, L. Stuart, K. VanWormer and L. Goldschmidt for supporting the running of the Institute for Protein Design. This work was supported by gifts from Microsoft (to D.L.S. and D.B.), The Donald and Jo Anne Petersen Endowment for Accelerating Advancements in Alzheimer’s Disease Research (to N.R.B.), Amgen (to J.L.W.), grant DE-SC0018940 MODO3 from the US Department of Energy Office of Science (to A.J.B. and D.B.), the National Institute of General Medical Sciences of the US National Institutes of Health under award number T32GM008268 (to D.L.S.), the National

Eye Institute of the National Institutes of Health under award number T32EY032448 (to Y.Y.), grant 5U19AG065156-02 from the National Institute for Aging (to D.B.), grant R01CA260415 from the National Cancer Institute (to C.C.L.), grant R35GM136297 from the National Institute of General Medical Sciences (to C.C.L.), the Institute for Rapid Antibody Engineering and Evolution as part of the Engineering+Health Initiative of the UCI Samueli School of Engineering (to C.C.L.), the Open Philanthropy Project Improving Protein Design Fund (to R.J.R. and D.B.), a grant (INV-010680) from the Bill and Melinda Gates Foundation (to J.L.W., C.W., E.L.S., K.D.C. and D.B.), an EMBO Postdoctoral Fellowship (grant number ALTF 292-2022; to J.L.W.), Howard Hughes Medical Institute COVID-19 Initiative (to C.W.), Defense Threat Reduction Agency grant HDTRA1-21-1-0007 (to B.H.), a National Science Foundation Training Grant (EF-2021552; to P.J.Y.L.), NERSC award BER-ERCAPO022018 (to P.J.Y.L.), a Grants for Resident Innovation and Projects award from the Children’s Hospital of Philadelphia (to R.A.), as part of the NextGen team supported by the Cancer Grand Challenges partnership funded by Cancer Research UK (CCCATF-2021/100002), the National Cancer Institute (CA278687-01) and The Mark Foundation for Cancer Research (to J.M.M. and N.G.S.), a grant (U19 AG065156) from the National Institute for Aging (to S.V.T.), a Washington Research Foundation Postdoctoral Fellowship program (to R.J.R.), the Defense Threat Reduction Agency Grant HDTRA1-21-1-0038 (to I.G.), the Howard Hughes Medical Institute (to N.R.B., R.J.R. and D.B.), a grant from the Institute for Basic Science IBS-R030-C1 (to H.M.K.), the Bill and Melinda Gates Foundation for Adjuvant Research (to C.C.), the Audacious Project at the Institute for Protein Design (to K.D.C. and D.B.) and an EMBO long-term fellowship (to B.I.M.W.). Figure 4 was created using BioRender (<http://biorender.com>).

**Author contributions** N.R.B., J.L.W. and R.J.R. conceived the study, and may change the order of their names for personal pursuits to best suit their own interests. N.R.B. and J.L.W. trained RFdiffusion and fine-tuned RoseTTAFold2. R.J.R., D.L.S. and R.B. led the experimental work, with help from E.L.S., P.J.Y.L., B.H., I.G., M.G.S., D.V., R.A., S.V.T., S.M.S., T.T.S. and K.O. J.M.M., N.G.S. and R.A.M. supervised the experimental work and provided reagents. A.J.B. led the negative stain electron microscopy and cryo-EM structural characterization work, with help from C.W. and K.D.C. J.L.W., N.R.B., D.L.S., R.A., C.C. and H.M.K. made the designs. D.L.S. and B.S. contributed additional code. D.L.S., R.B. and R.J.R. did the retrospective AlphaFold3 analysis. J.L.W., R.J.R. and B.I.M.W. devised the library assembly strategy. S.C. and Y.S. purified the target proteins. Y.Y. performed the OrthoRep experiments under the guidance and supervision of C.C.L. J.L.W., R.J.R. and D.B. co-managed the project. J.L.W., D.B., R.J.R., N.R.B. and A.J.B. wrote the manuscript. All authors read and contributed to the manuscript.

**Competing interests** N.R.B., J.L.W., R.J.R., A.J.B., C.W., P.J.Y.L., B.H. and D.B. are co-inventors on US provisional patent number 63/607,651, which covers the computational antibody design pipeline described here. N.R.B., J.L.W., P.J.Y.L. and B.H. are currently employed by Xaira Therapeutics. N.R.B., J.L.W., P.J.Y.L., B.H., R.J.R., A.J.B. and C.W. have received payments relating to the licensing of the inventions described here to Xaira Therapeutics. C.C.L. is a co-founder of K2 Therapeutics, which uses OrthoRep in antibody engineering and evolution. The other authors declare no competing interests.

## Additional information

**Supplementary information** The online version contains supplementary material available at <https://doi.org/10.1038/s41586-025-09721-5>.

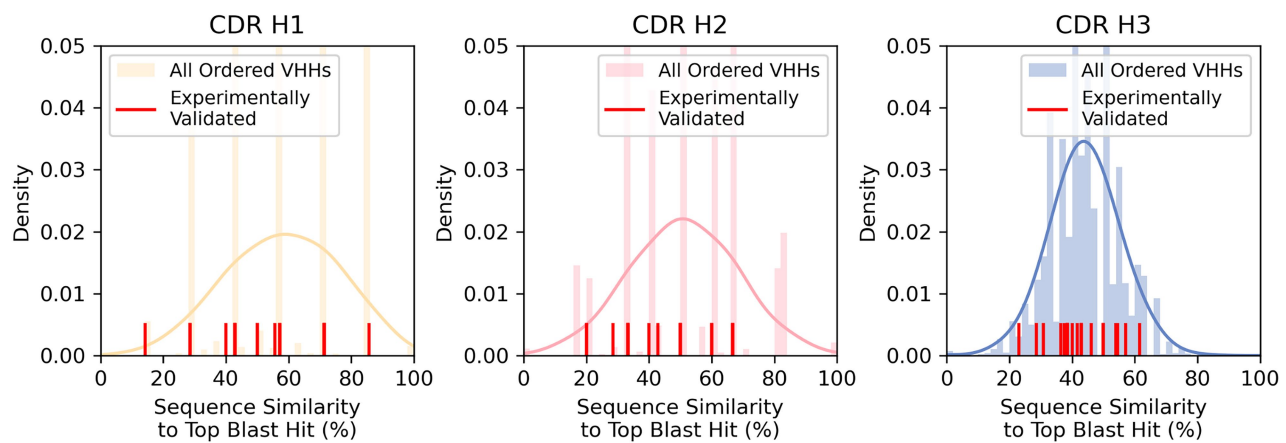
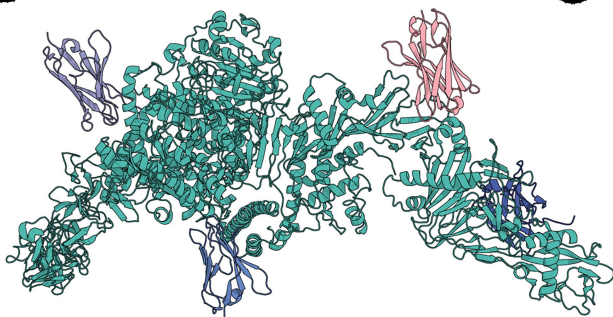
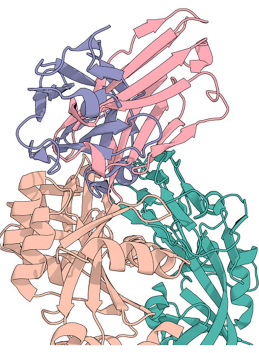
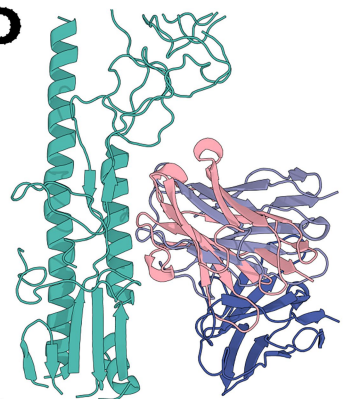
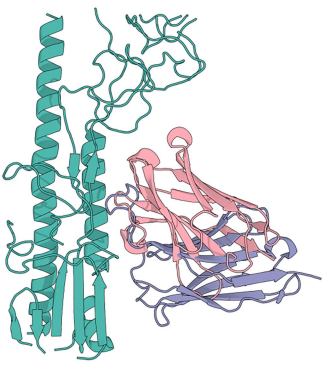
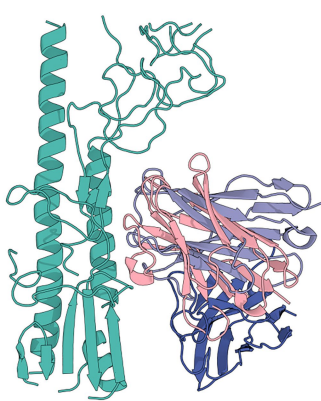
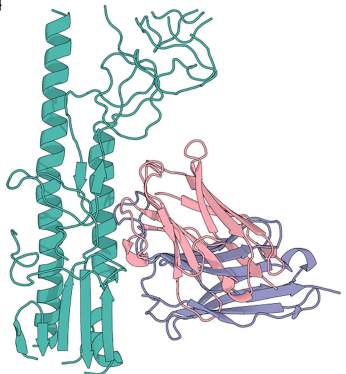
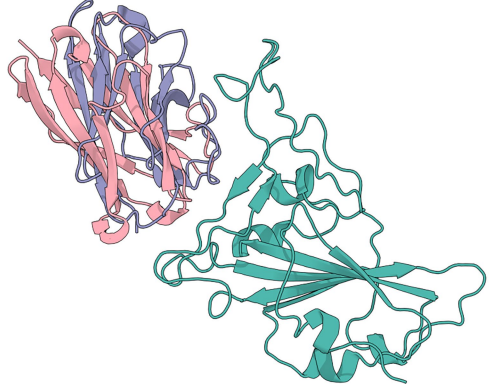
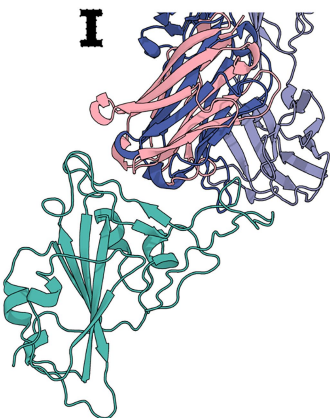
**Correspondence and requests for materials** should be addressed to Joseph L. Watson, Robert J. Ragotte or David Baker.

**Peer review information** *Nature* thanks Hayian Liu, Yufeng Liu, Carlos Outeiral, Amalio Telenti and the other, anonymous, reviewer(s) for their contribution to the peer review of this work. Peer review reports are available.

**Reprints and permissions information** is available at <http://www.nature.com/reprints>.

**A**

## Sequence Similarity of Designed VHHS to the Training Dataset

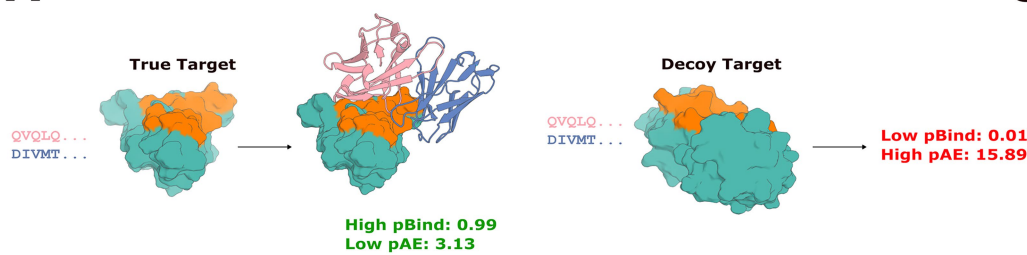
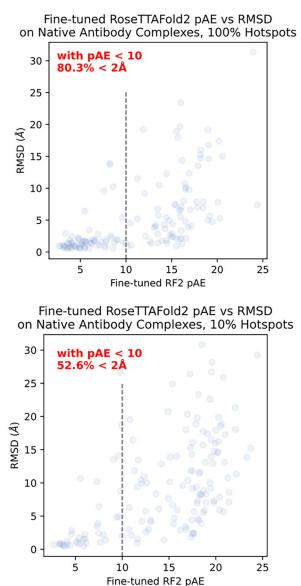
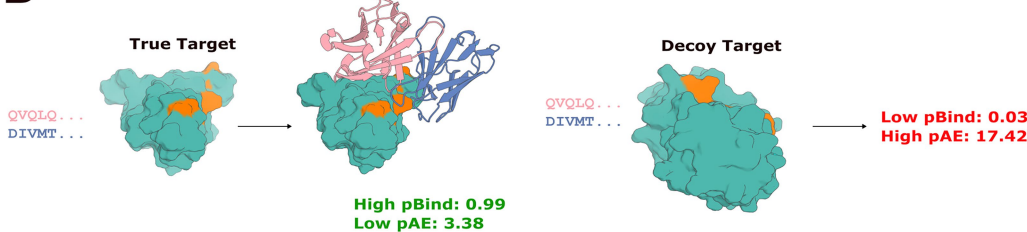
**B****C****D****E****F****G****H****I**

# Article

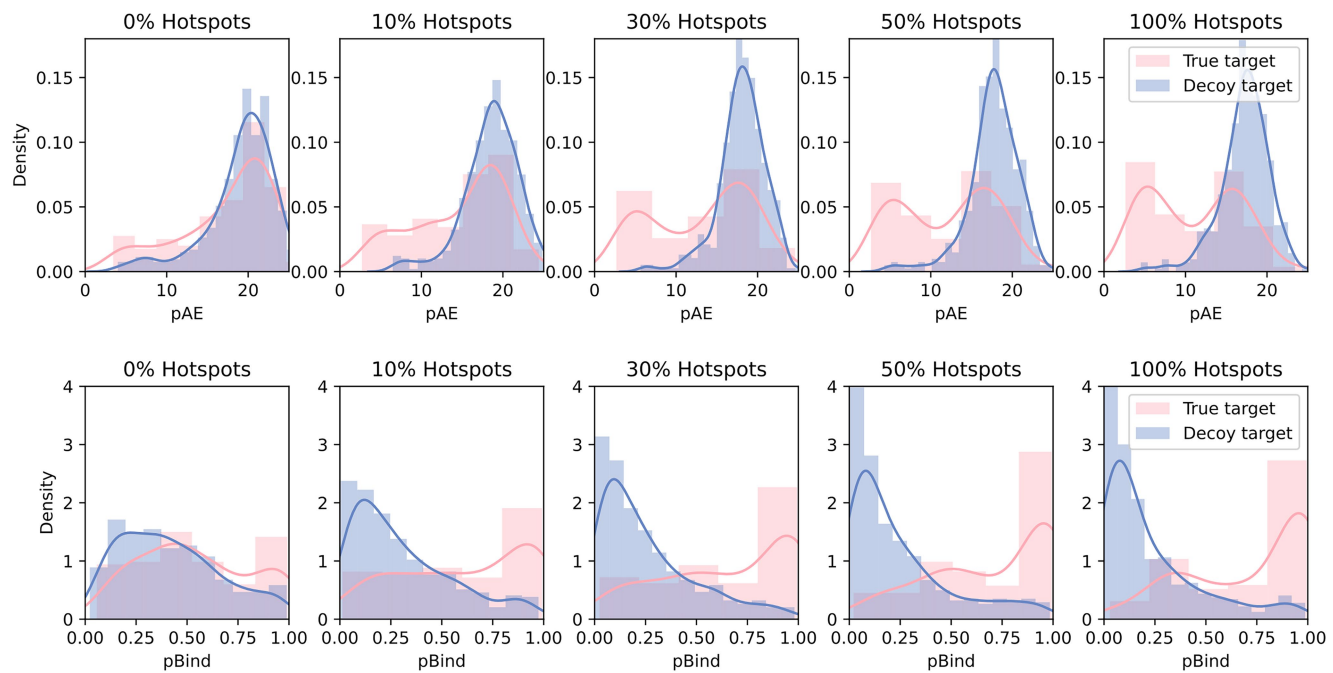
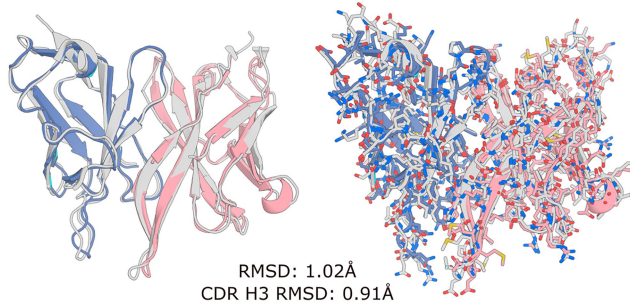
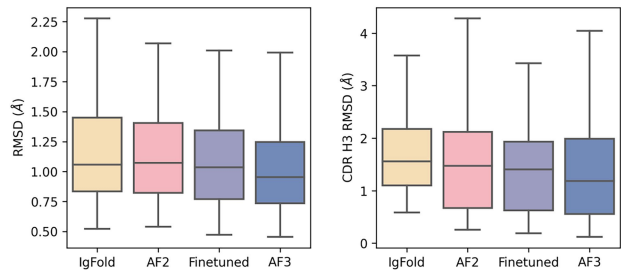
## Extended Data Fig. 1 | Designed VHH are dissimilar to the training dataset.

**A)** Designed VHH sequences are distinct from the training dataset. Blastp<sup>49</sup> was used to find hits against the SAbDab<sup>50</sup>, and the similarity of the CDR loops in the top blast hit were reported for all VHHs experimentally tested in this study. Note also that the 28 VHHs confirmed to bind their targets by SPR do not show enhanced similarity to the training set (red lines). **B-I)** Designed VHH are structurally distinct from immunoglobulins binding (when existent) to the epitopes used in this study. For each of the highest affinity VHHs identified for each target, and the structurally characterized influenza HA VHH, the closest complex in the PDB is shown. Designed VHHs (pink) are shown in complex with their designed target (teal and tan). The closest complex was identified visually (Methods). **B)** Designed TcdB VHH aligned against 3 VHHs from PDB ID: 6OQ5

(shades of blue). The designed TcdB VHH binds to a site for which no antibody or VHH structure exists in the PDB. **C)** Designed RSV Site III VHH aligned against VHH from PDB ID: 5T0J (blue). **D)** Highest affinity designed influenza HA VHH aligned against Fv from PDB ID: 8DIU (shades of blue). **E)** Highest affinity designed influenza HA VHH aligned against VHH from PDB ID: 6FYT (blue). **F)** Structurally characterized (cryoEM) designed influenza HA VHH aligned against Fv from PDB ID: 8DIU (shades of blue). **G)** Structurally characterized (cryoEM) designed influenza HA VHH aligned against VHH from PDB ID: 6FYT (blue). **H)** Designed SARS-CoV-2 VHH aligned against VHH from PDB ID: 8Q94 (blue). **I)** Designed SARS-CoV-2 VHH aligned against FAb from PDB ID: 7FCP (shades of blue).

**A****C****B****D**

Ability of fine-tuned RoseTTAFold2 to discriminate True targets from Decoys

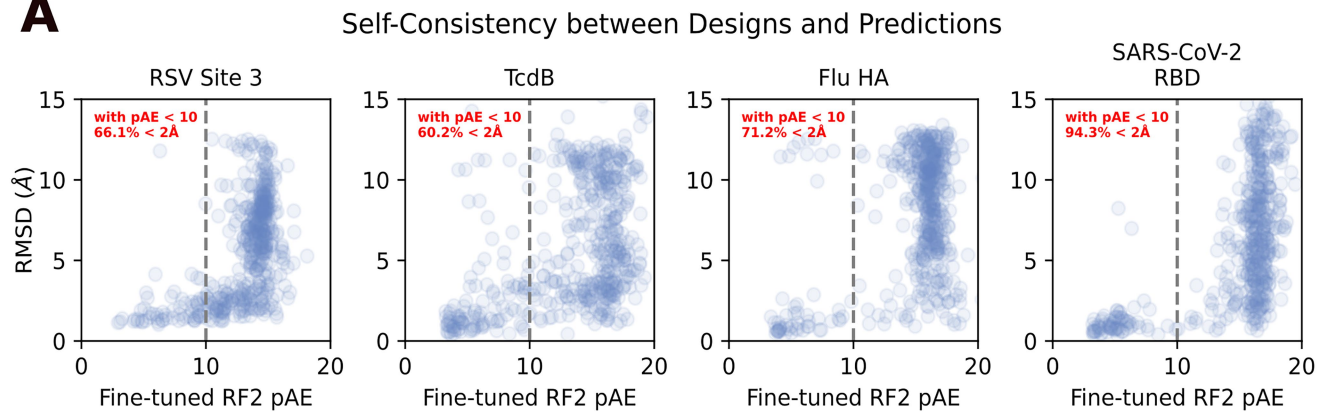
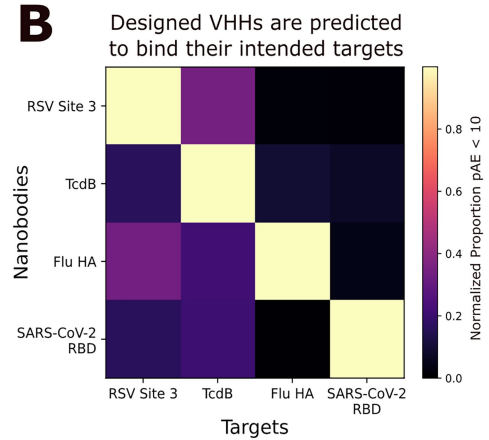
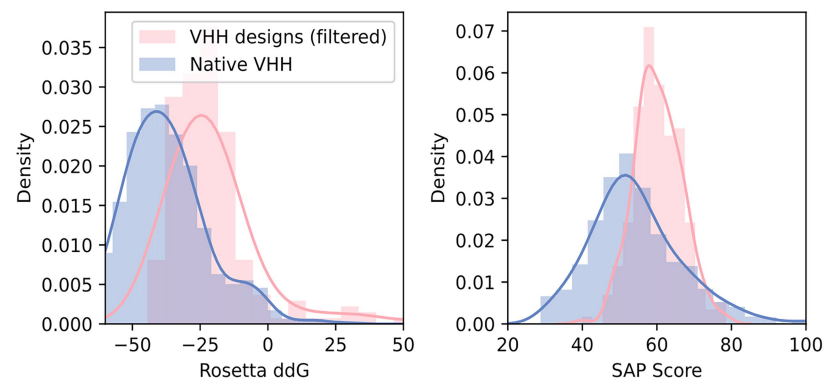
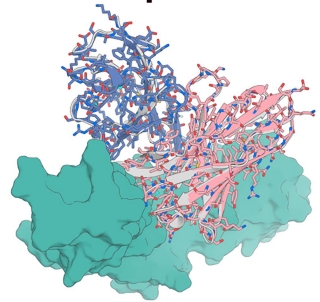
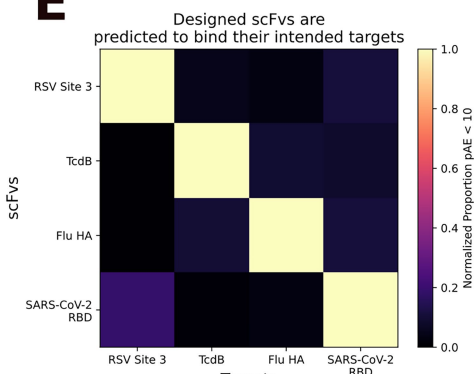
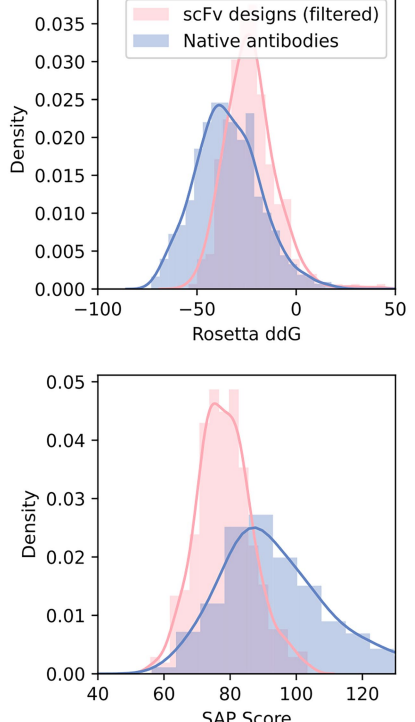
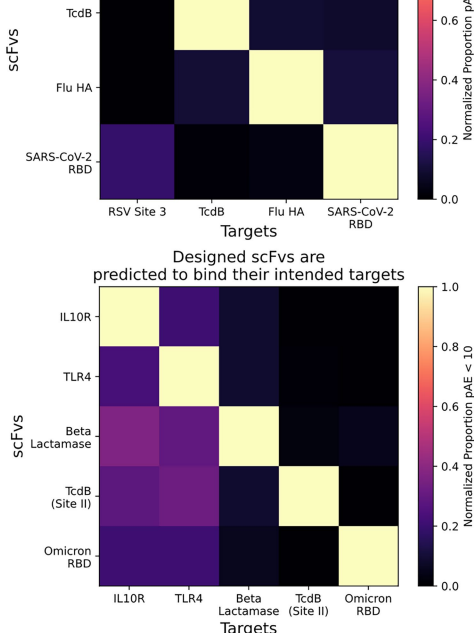
**E****F**

**Extended Data Fig. 2** | See next page for caption.

## Article

**Extended Data Fig. 2 | Fine-tuned RoseTTAFold2 can distinguish true complexes from decoy complexes.** **A-B**) Cherry-picked example of RoseTTAFold2 correctly distinguishing a “true” from a “decoy” complex. The sequence of antibody 7Y1B was provided either with the correct (PDB ID: 7Y1B) or decoy (PDB ID: 8CAF) target. Both with 100% (**A**) or 10% (**B**) of “hotspots” provided, RF2 near-perfectly predicts binding (top row) or non-binding (bottom row). **C**) Fine-tuned RoseTTAFold2 reliably predicts its own accuracy. Correlation between RF2 predicted aligned error (pAE) and RMSD to the native structure with 100% (top) or 10% (bottom) of “hotspot” residues provided. With mean pAE <10, 80.3% of structures are within 2 Å when 100% of “hotspots” are provided (along with the holo target structure), with this falling to 52.6% when only 10% of hotspots are provided. **D**) Quantification of the fine-tuned RF2’s ability to distinguish true targets from decoy targets with both pAE (top row) and pBind (bottom row). Note that this ability depends on the proportion of “hotspots” provided. Without any “hotspots” provided, RF2 is hardly predictive,

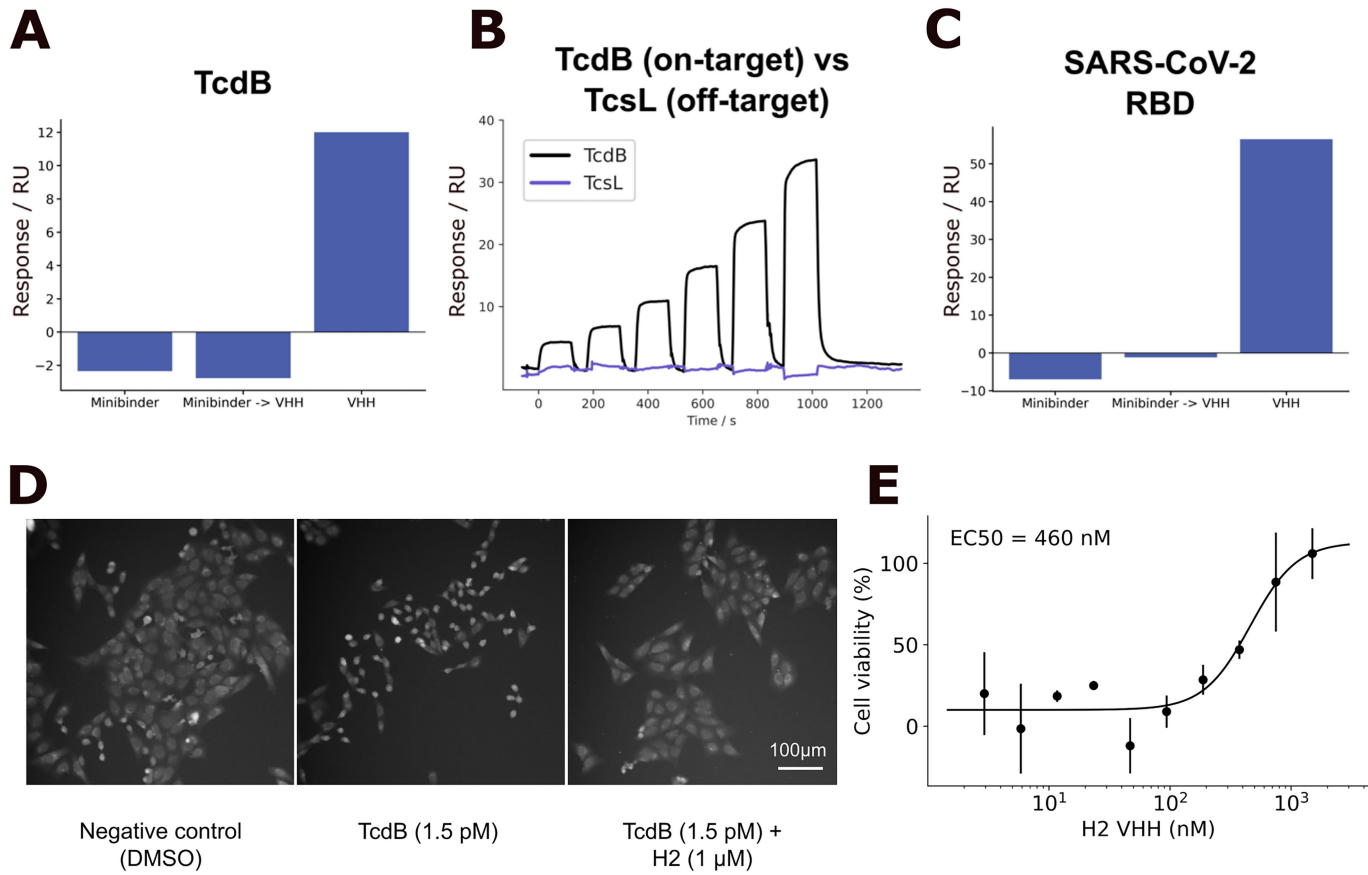
because RF2 without privileged information is quite rarely confident or accurate in its antibody complex predictions. **E-F**) Fine-tuned RoseTTAFold is also performant at antibody monomer prediction. 86 antibodies released after the RF2, AlphaFold and IgFold training dataset date cutoff (January 13th, 2023) that share <30% target sequence similarity to any antibody complex released prior to this date were predicted as monomers with either fine-tuned RF2, IgFold, AF2 and AF3. **E**) The median Fv quality prediction (by overall RMSD) of fine-tuned RF2, of (PDB ID: 8GPG), with (right) and without (left) sidechains shown (gray: native; colors: prediction). While the backbone RMSD is close to the true structure, some sidechains are incorrectly positioned. **F**) Fine-tuned RF2 slightly outperforms IgFold at prediction accuracy. Overall prediction accuracy is slightly improved in fine-tuned RF2 vs IgFold ( $p = 0.026$ , Student’s Paired T-test), with greater improvements in CDR H3 prediction accuracy ( $p = 0.0003$ , Student’s Paired T-test).

**A****B****C****D****IL10 Receptor- $\alpha$** **E****F**

# Article

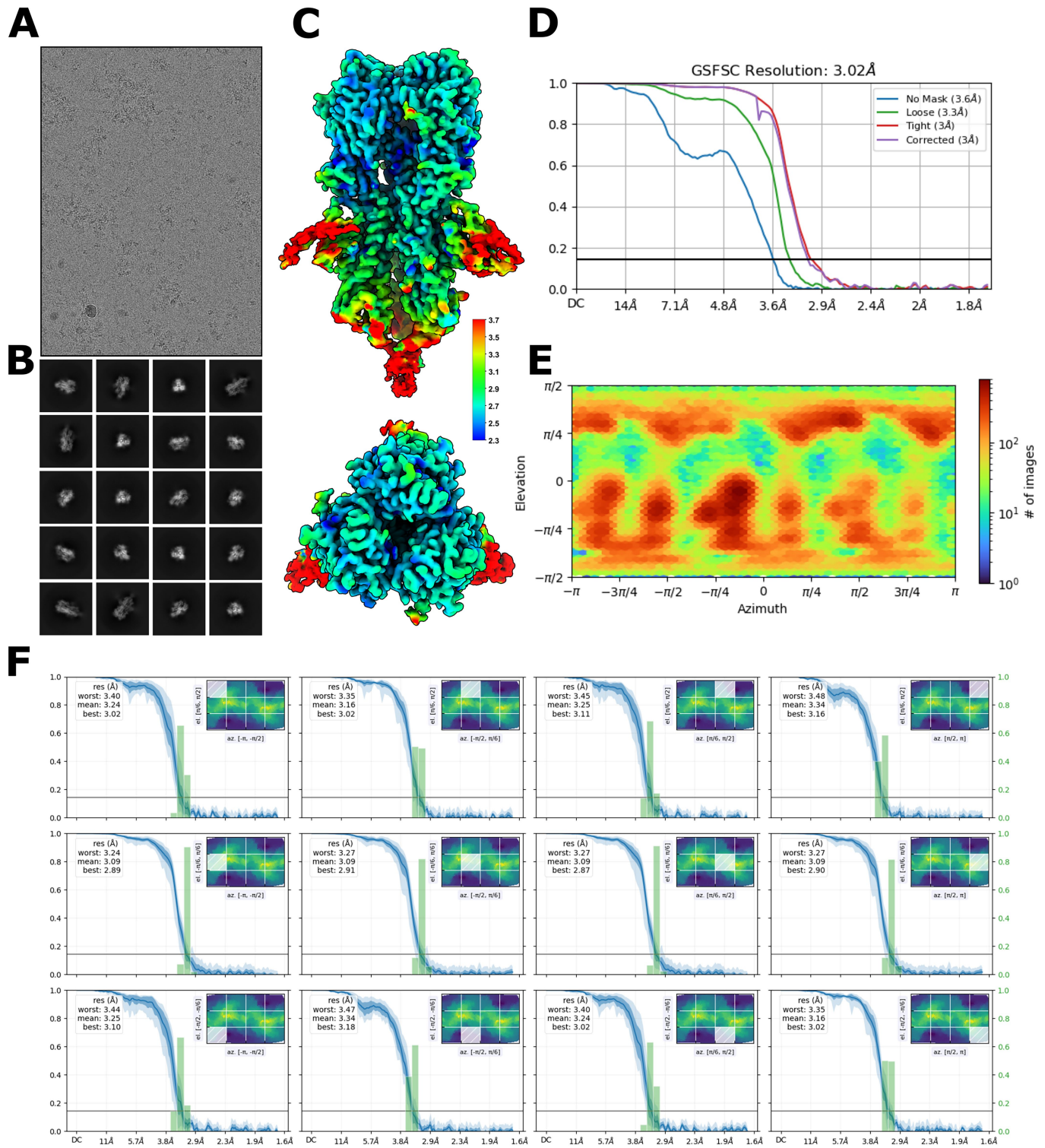
**Extended Data Fig. 3 | Fine-tuned RoseTTAFold2 recapitulates design structures and computationally demonstrates specificity of VHHS for their targets. A-C: VHH Design.** **A)** Comparison of RF2 pAE and RMSD of the prediction to the design model. A significant fraction of designs are re-predicted by RF2 (given 100% of “hotspots”), and pAE correlates well with accuracy to the design model. **B)** RF2 can be used to assess quality of designed VHHS. Providing the VHH sequence with the true target structure (used during design) leads to higher rates of high-confidence predictions than predicting the same sequence with a decoy structure (not used in design), as assessed by the fraction of predictions with pAE <10 (normalized to the fraction of predictions with pAE <10 for that target with its “correct” VHH partners). In these experiments, the true or decoy target was provided along with 100% of hotspot residues, with those hotspot residues derived from the target with its “true” designed VHH bound. **C)** Orthogonal assessment of designed VHHS with Rosetta demonstrates that the interfaces of RF2-approved (RMSD < 2 Å to design model, pAE <10) VHH designs have estimated binding energy (ddG) only slightly less favourable than native VHH (left) and slightly higher spatial

aggregation propensity (SAP) score as compared to natives (right). **D-F: scFv design.** **D)** RFdiffusion was used to generate scFv designs using the framework from Herceptin (hu4D5-8), which has been used to make scFvs previously<sup>31</sup>. Five targets were chosen (IL10 Receptor- $\alpha$ , TLR4,  $\beta$ -lactamase, TcdB and SARS-CoV-2 (omicron) RBD (PDB IDs: 6X93, 4G8A, 4ZAM, 7ML7, 7WPC). Shown are two examples with close agreement between the design model and the fine-tuned RF2 prediction (RMSD (Å): 0.60, 0.43; pAE: 4.73, 3.52). Gray: designs, Pink: RF2 prediction. **E)** Top: Against the same four targets to which VHHS were successfully designed, fine-tuned RF2 also predicts good specificity of designed scFvs to the designed target vs decoy targets. Bottom: against the set of five aforementioned targets, fine-tuned RF2 similarly predicts high scFv specificity to the designed target vs decoy targets. **F)** Orthogonal assessment of designed scFvs with Rosetta demonstrates that the interfaces of RF2-approved (RMSD < 2 Å to design model, pAE <10) scFv designs have low ddG (top; only slightly worse than native Fabs) and lower spatial aggregation propensity (SAP) score as compared to natives (bottom).



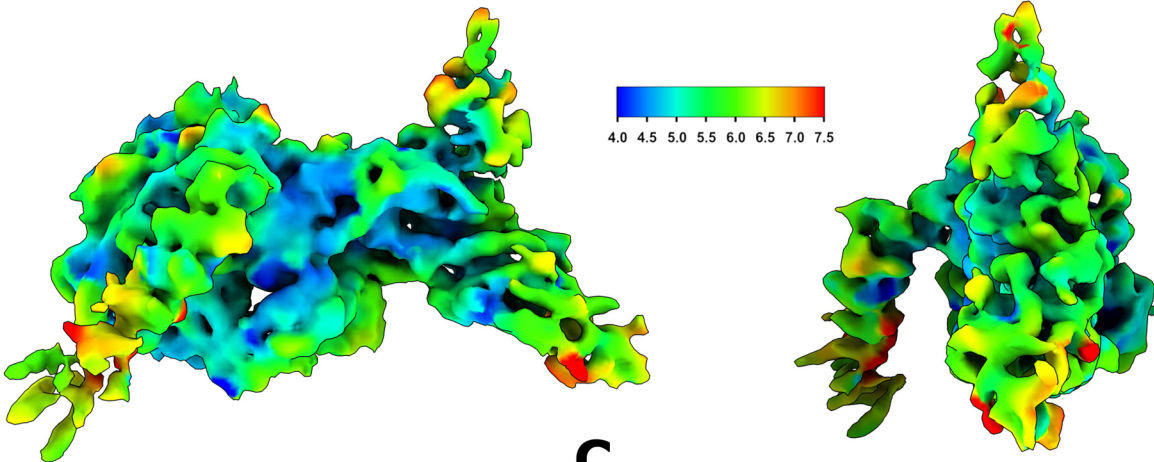
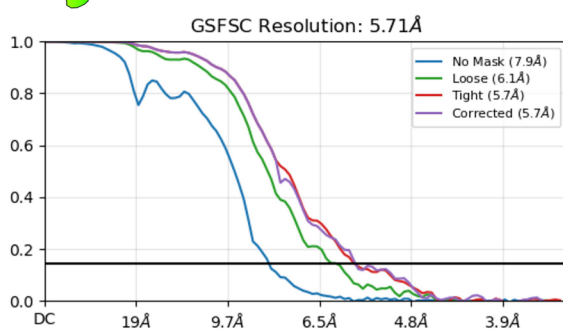
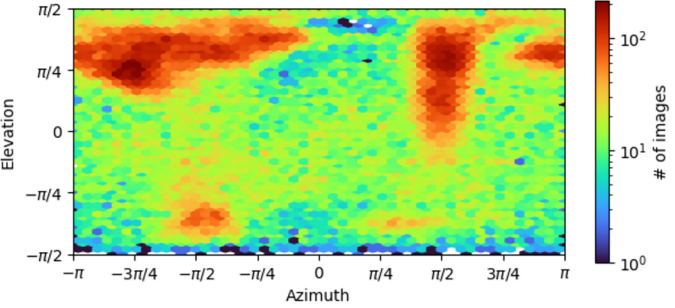
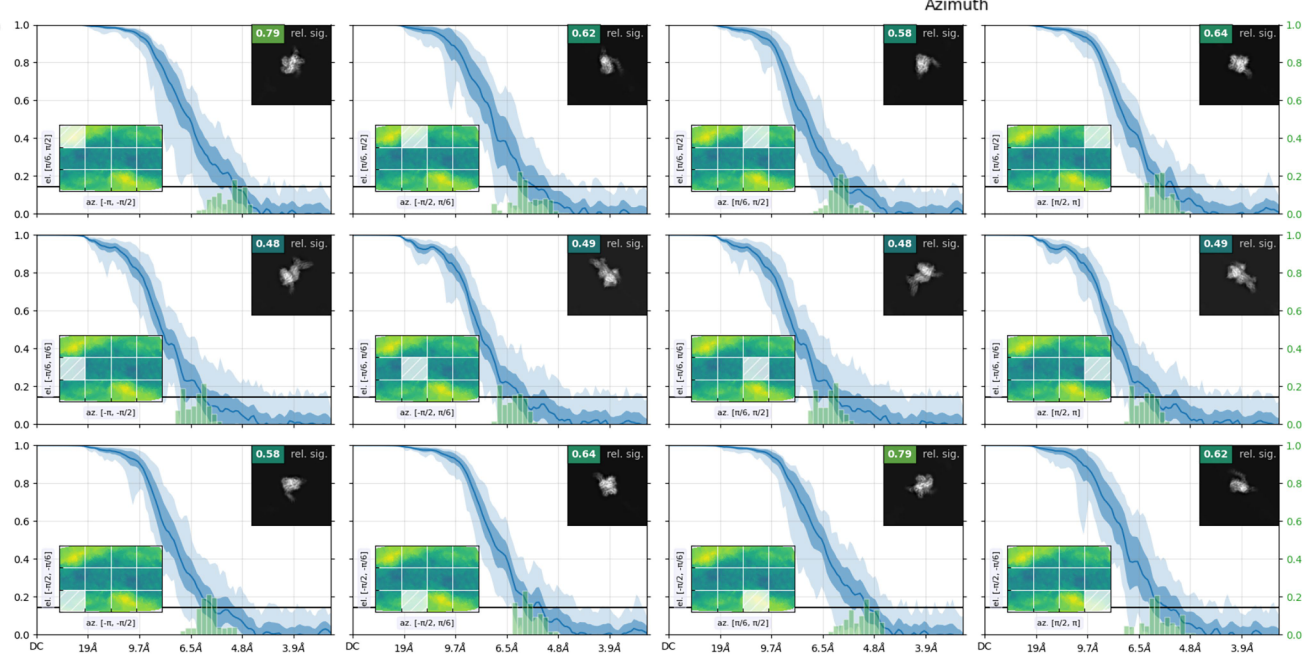
**Extended Data Fig. 4 | Analysis of SPR Competition Assays.** **A)** TcdB VHH binds to the correct epitope. The average response during VHH injection normalized to the response immediately preceding VHH injection for TcdB VHH competition with minibinder fz48. When the minibinder is injected prior to the VHH (middle bar), the VHH no longer binds, confirming competition with the minibinder. **B)** TcdB VHH is specific. No binding is observed to the closely related *Clostridium sordellii* TcsL toxin, indicating that it is binding through specific interactions. **C)** SARS-CoV-2 RBD VHH competition with the minibinder AHB2. As in (A), when minibinder is injected prior to the VHH injection (middle bar) no response is observed. When the VHH is injected without a preceding minibinder injection (right bar), the VHH binds as expected. (A) and (C) are the quantification from the rightmost panels of Fig. 2a,b. **D)** Brightfield microscopy of Vero CSPG4 KO cells treated with vehicle, TcdB alone or TcdB + VHH after 24 h. **E)** Neutralization of TcdB by VHH\_TcdB\_H2 in CSPG4 KO Vero cells. Cell viability is measured after 48 h. Points indicate the mean and error bars are the standard deviation across two independent replicates.

# Article



**Extended Data Fig. 5 | Cryo-EM structure determination statistics for a de novo designed VHH bound to an influenza HA trimer.** **A)** Representative raw micrograph showing ideal particle distribution and contrast. **B)** 2D Class averages of Influenza H1+designed VHH with clearly defined secondary structure elements and a full-sampling of particle view angles. **C)** Cryo-EM local

resolution map calculated using an FSC value of 0.143 viewed along two different angles. Local resolution estimates range from  $-2.3 \text{ \AA}$  at the core of H1 to  $-3.7 \text{ \AA}$  along the periphery of the designed VHH. **D)** Global resolution estimation plot. **E)** Orientational distribution plot demonstrating complete angular sampling. **F)** Orientational diagnostics data.

**A****B****C****D**

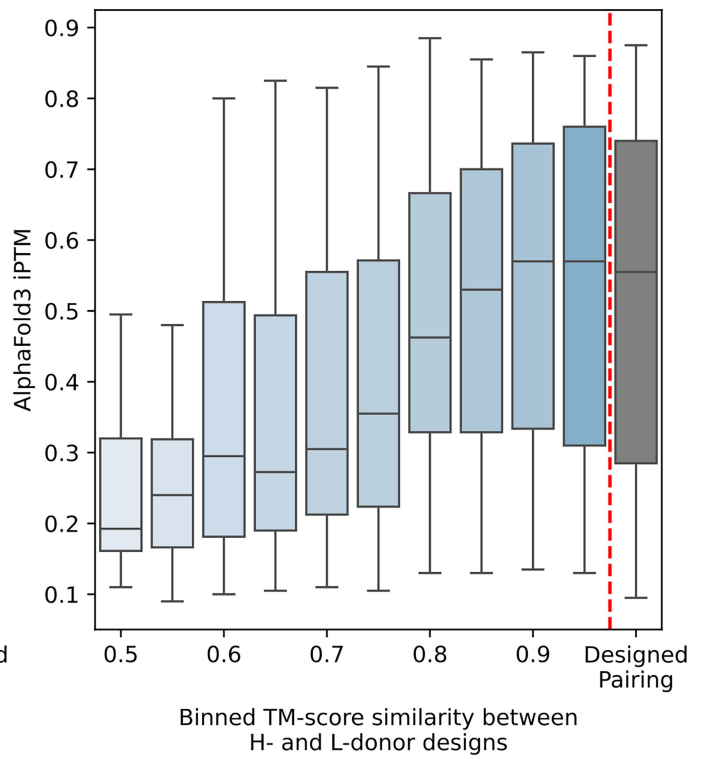
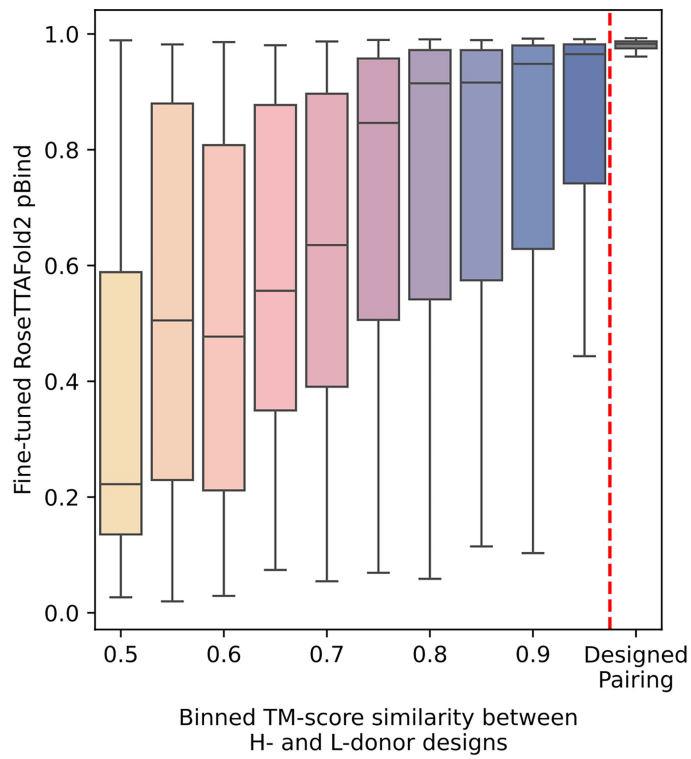
**Extended Data Fig. 6 | Final Local Refinement CryoEM statistics for OrthoRep Affinity Matured TcdB VHH, VHH\_TcdB\_H2\_ortho in complex with TcdB.** Local refinement and masking used to reduce noise from His tag and improve resolution. **A)** Local Resolution map (Å), calculated using an FSC

value of 0.143 viewed along two different angles. **B)** Global Fourier Shell Correlation plot, Local Refinement. **C)** Orientational distribution plot. **D)** Oriental diagnostics data.

# Article

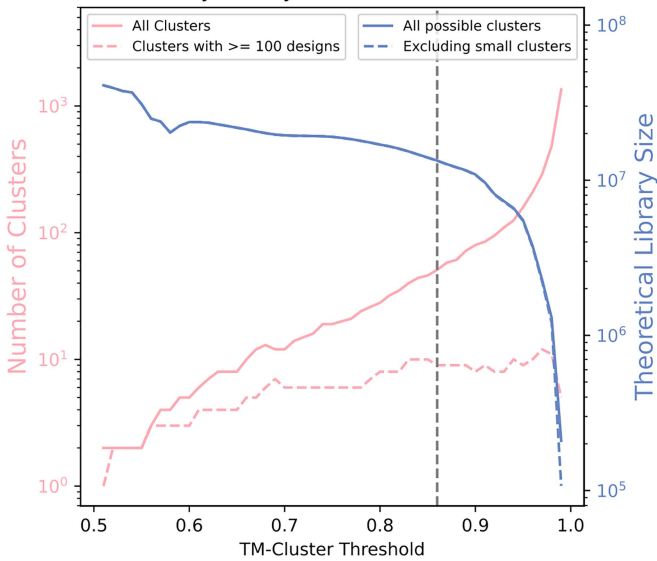
**A**

Structurally similar designs yield compatible Heavy and Light chains



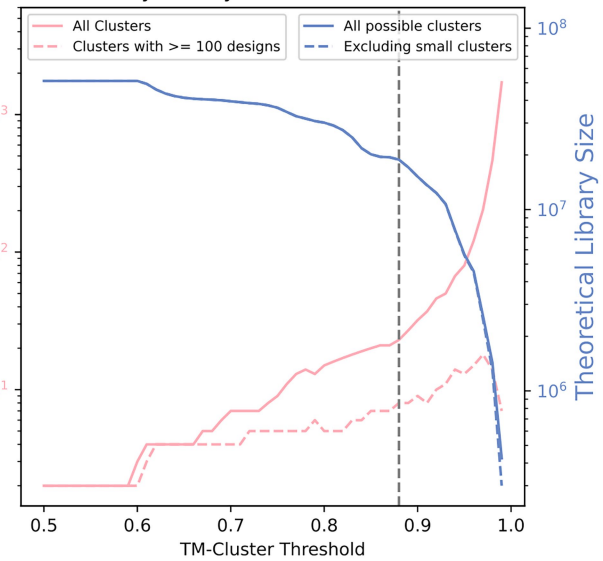
**B**

Number of TcdB scFv Clusters and Library Size by TM-Cluster Threshold



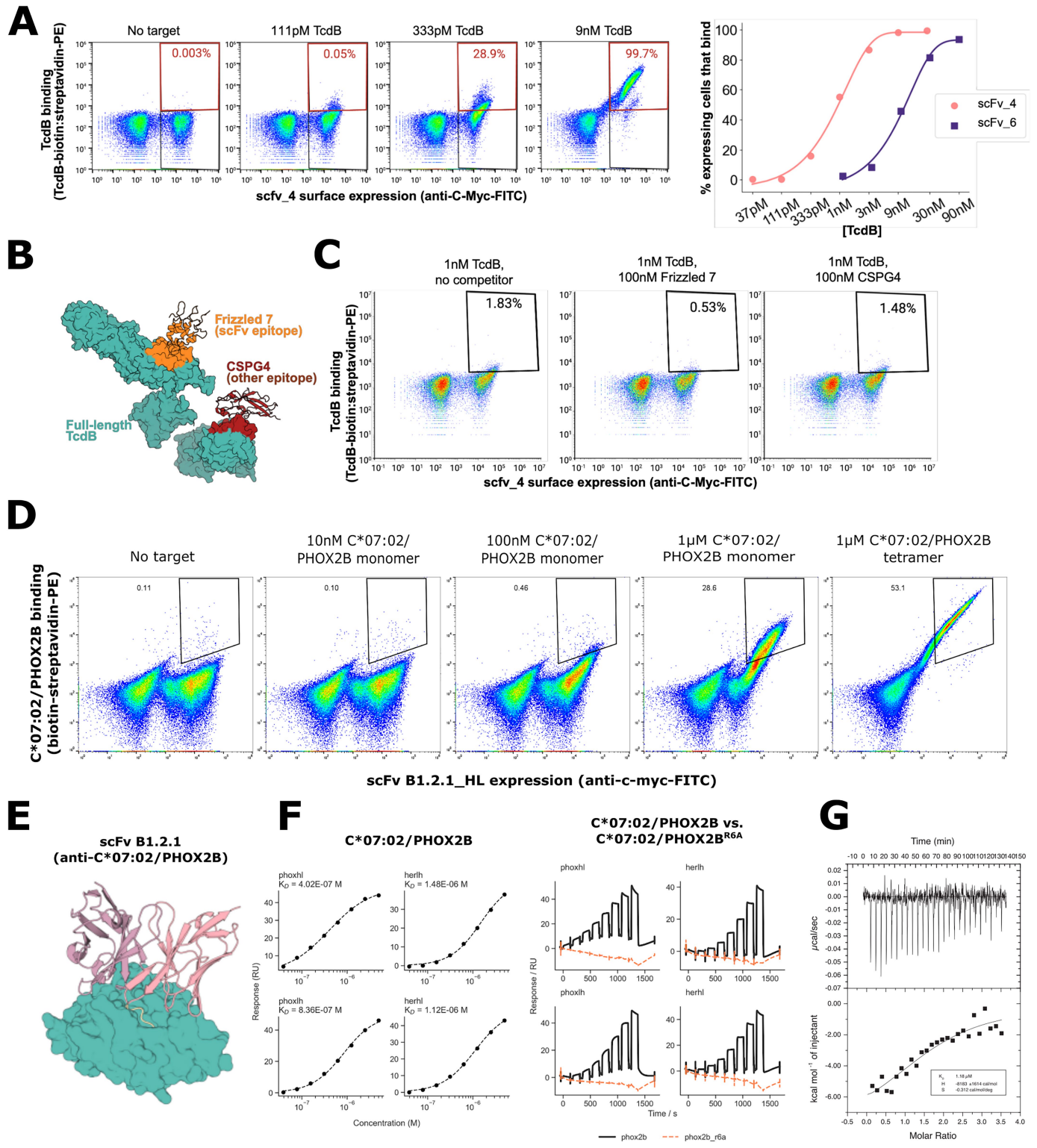
**C**

Number of Phox2B scFv Clusters and Library Size by TM-Cluster Threshold



**Extended Data Fig. 7 | Computational validation of the structure-based combinatorial assembly strategy.** Structure-based design permits the rational combinatorial assembly of heavy and light chains, assembling only heavy and light chains from structurally similar pairs. **A**) Fine-tuned RoseTTAFold (left), and AlphaFold3 (right) validate that pairing heavy and light chains from structurally similar (i.e. high pairwise TM score) designs yields scFVs that are more likely to be predicted to bind with high confidence (RF2 pBind, left; AF3 ipTM, right) than heavy and light chains from structurally-dissimilar (low pairwise TM score) designs. Note that the extremely high pBind distribution of the “designed pairings” (rightmost bar of left plot) is an artifact of those designs being specifically filtered for high pBind scores prior to the library being

ordered. **B-C)** combinatorial assembly leads to dramatically larger library sizes. Plots show the number of clusters (pink) at different TM score similarity thresholds for TcdB (left) and Phox2b (right) scFvs. For the amplification strategy to work, each “cluster” becomes a PCR subpool, requiring independent PCR reactions (3 per subpool). Hence, we limit ourselves to large subpools ( $\geq 100$  designs), which maximizes the combinatorial amplification for the amount of additional library assembly work. We additionally plot the theoretical library size for each target (blue), calculated as  $\text{number\_of\_clusters} \times \text{cluster\_size}^2$ . Gray lines indicate the TM threshold chosen for library assembly, where library sizes approximately match the transformation efficiency of yeast ( $10^7$ )<sup>52</sup>.



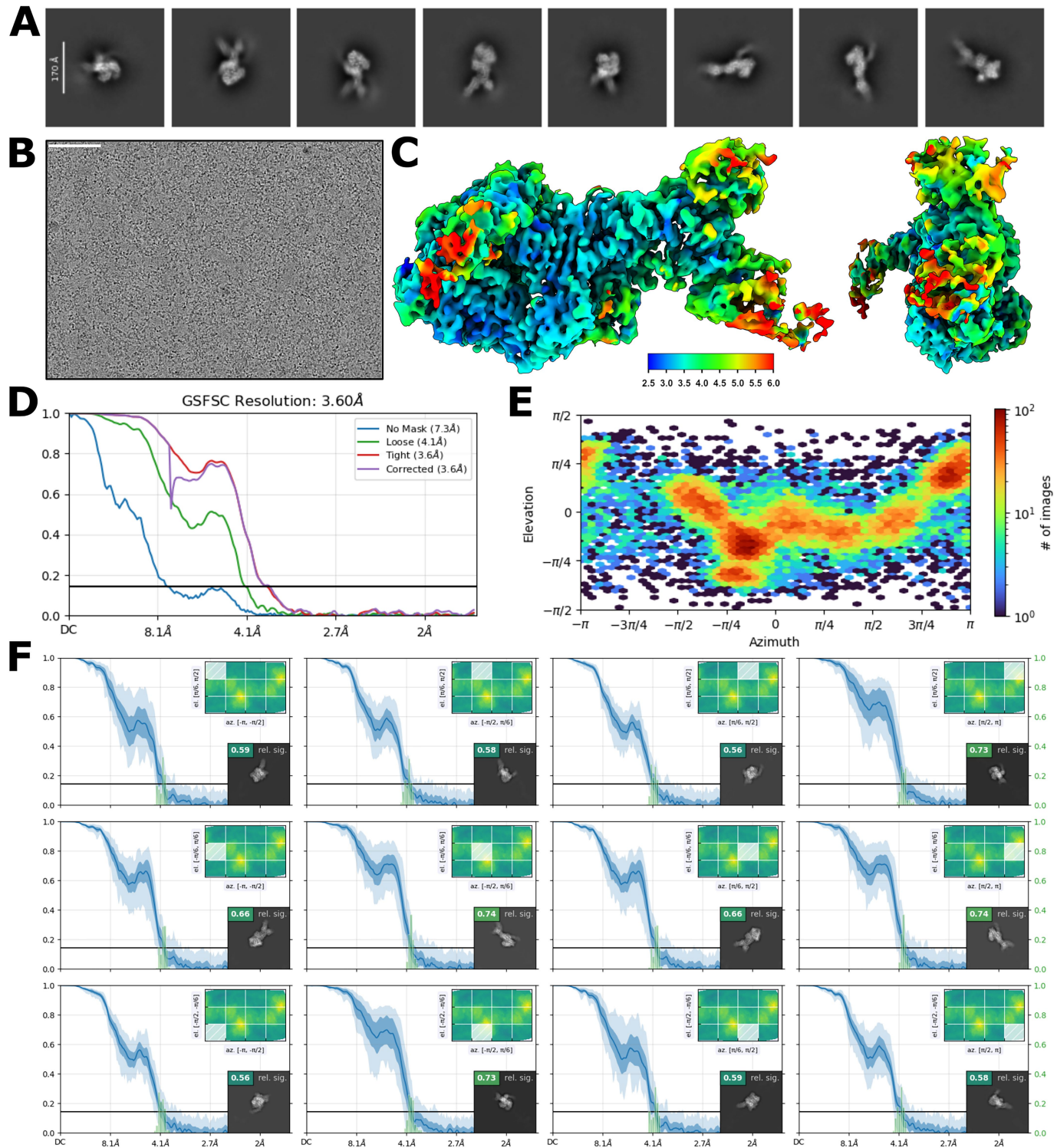
Extended Data Fig. 8 | See next page for caption.

# Article

## Extended Data Fig. 8 | Characterization of TcdB- and Phox2B-binding scFvs. A-C: TcdB-binding scFvs.

**A**) (left) Results of flow cytometry of yeast samples displaying scFv4-C-Myc construct. Each sample was treated with a titration of soluble biotinylated TcdB fragment (1285-1804) (bn-TcdB) concentrations and visualized with anti-C-Myc FITC + SAPE. (right) Percentage of expressing cells which are within the gate increase with bn-TcdB concentration. **B**) scFvs were designed to bind to the Frizzled epitope and therefore should compete with Frizzled-7. Designed scFvs should not compete with CSPG4, which binds at a different epitope on full-length TcdB. **C**) Yeast displaying scFv4-C-Myc were incubated with 1 nM TcdB and either no competitor, 100 nM Frizzled-7, or 100 nM CSPG4. Binding signal specifically decreases when Frizzled-7 is added, supporting that scFv4 binds at the Frizzled-7 epitope. Binding signal does not significantly decrease when CSPG4 is added. **D-G: Phox2B-binding scFvs.** **D)** C\*07:02/PHOX2B titration results with yeast surface display of anti-C\*07:02/PHOX2B scFv B1.2.1, tested in the “HL” orientation with a (G4S)3 linker. For the tetramer condition, the biotinylated

C:07:02/PHOX2B pH LA was tetramerized on streptavidin-PE (SAPE) prior to validation. The negative control is yeast incubated in the same concentrations of SAPE and FITC used in the experimental conditions in the absence of target. **E)** AF3 prediction of construct B1.2.1 docked to C\*07:02/PHOX2B. **F)** Left: Surface plasmon resonance (SPR) data characterizing binding of B1.2.1 in the HL and LH orientations in the 10LH-based framework (“phox” prefix, left column) and the trastuzumab framework (“her” prefix, right column). B1.2.1 binds with approximately 1  $\mu$ M affinity. Right: SPR data characterizing on-target binding of C\*07:02/PHOX2B (“phox2b”) versus the same HLA bound to the R6A mutant of PHOX2B (“phox2b\_r6a”). The results indicate specific binding to the intended target. **G)** Representative ITC titration of HLA-C\*07:02/PHOX2B (30  $\mu$ M) into a sample containing 2  $\mu$ M herceptin\_VLVH-His-Avi binder. Both samples contain 1 mM excess of PHOX2B peptide, to prevent the formation of empty HLA. The black line is the fit of the isotherm. Fitted values for KD,  $\Delta H$ , and  $\Delta S$  were determined using a 1-site binding model.



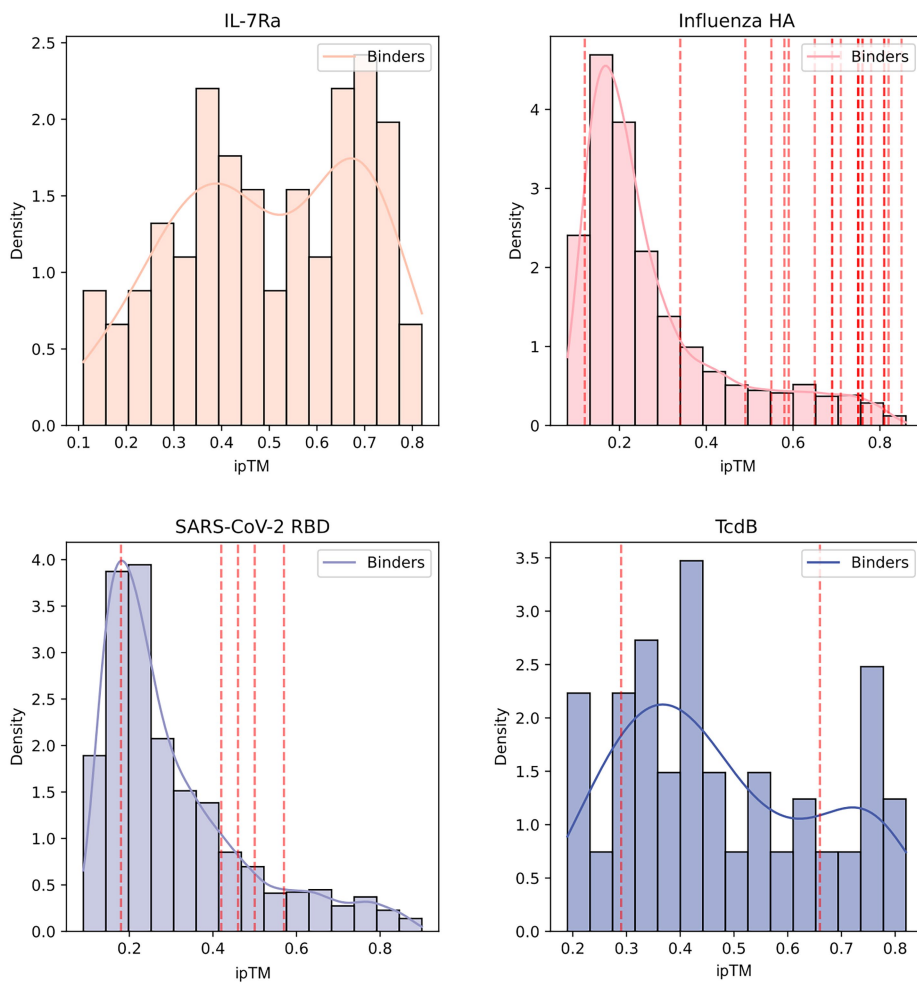
#### Extended Data Fig. 9 | CryoEM statistics for TcdB in complex with scFv6.

10,897 movies were collected on a Glacios with a K3 detector. Thin ice was targeted for imaging, and only extended TcdB were observed. Heterogeneous refinement and apo structure were used to sort scFv bound TcdB (41,837 particles) and unbound apo TcdB (14,384 particles). **A**) 2D Class Averages. **B**) Representative

micrograph **C**) Local Resolution map (Å), calculated using an FSC value of 0.143 viewed along two different angles **D**) Global Fourier Shell Correlation plot, Non Uniform Refinement **E**) Orientational distribution plots. **F**) Orientational diagnostics data.

**A**

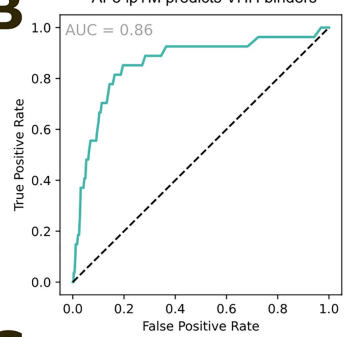
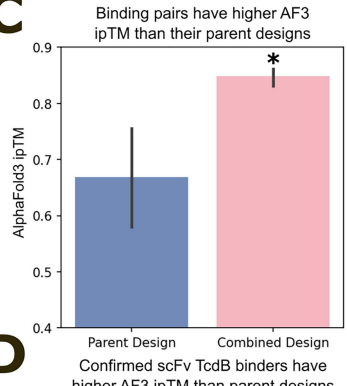
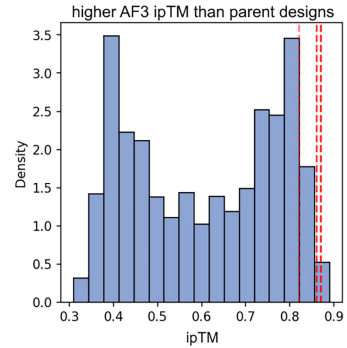
## AF3 ipTM distributions of designed VHH

**Extended Data Fig. 10 | AlphaFold3 retrospectively predicts binders.**

**A**) ipTM distributions of design VHH libraries against 4 targets. Red lines indicate validated binders. **B**) ROC curve demonstrating strong retrospective predictive power of AF3 at discriminating designed VHH binders from non-binders (AUC = 0.86). Note though that this plot is dominated by influenza HA binders, which are more numerous than confirmed binders to SARS-CoV-2 RBD and TcdB. **C-D)** Similar retrospective analyses of TcdB scFv binders.

**B**

## AF3 ipTM predicts VHH binders

**C****D**

These binders were assembled combinatorially from structurally similar “parent” designs. The successfully-binding combined designs have significantly higher AF3 ipTM scores than the parent designs from which they emanate (**C**, 6 binders from 12 parent designs; two-sided Students t-test;  $p = 0.0025$ ), and from the parental library as a whole (**D**). These analyses indicate the utility of AF3 for antibody design filtering.

David Baker, Joseph L. Watson, Robert J.

Corresponding author(s): Ragotte

Last updated by author(s): Joseph L. Watson

## Reporting Summary

Nature Portfolio wishes to improve the reproducibility of the work that we publish. This form provides structure for consistency and transparency in reporting. For further information on Nature Portfolio policies, see our [Editorial Policies](#) and the [Editorial Policy Checklist](#).

### Statistics

For all statistical analyses, confirm that the following items are present in the figure legend, table legend, main text, or Methods section.

n/a Confirmed

- The exact sample size ( $n$ ) for each experimental group/condition, given as a discrete number and unit of measurement
- A statement on whether measurements were taken from distinct samples or whether the same sample was measured repeatedly
- The statistical test(s) used AND whether they are one- or two-sided  
*Only common tests should be described solely by name; describe more complex techniques in the Methods section.*
- A description of all covariates tested
- A description of any assumptions or corrections, such as tests of normality and adjustment for multiple comparisons
- A full description of the statistical parameters including central tendency (e.g. means) or other basic estimates (e.g. regression coefficient) AND variation (e.g. standard deviation) or associated estimates of uncertainty (e.g. confidence intervals)
- For null hypothesis testing, the test statistic (e.g.  $F$ ,  $t$ ,  $r$ ) with confidence intervals, effect sizes, degrees of freedom and  $P$  value noted  
*Give  $P$  values as exact values whenever suitable.*
- For Bayesian analysis, information on the choice of priors and Markov chain Monte Carlo settings
- For hierarchical and complex designs, identification of the appropriate level for tests and full reporting of outcomes
- Estimates of effect sizes (e.g. Cohen's  $d$ , Pearson's  $r$ ), indicating how they were calculated

*Our web collection on [statistics for biologists](#) contains articles on many of the points above.*

### Software and code

Policy information about [availability of computer code](#)

Data collection This paper developed and uses custom code available at <https://github.com/RosettaCommons/RFantibody>. Additionally, it used ProteinMPNN, AlphaFold2, AlphaFold3, IgFold, TMalign, Protein-Protein BLAST 2.11.0+, SerialEM

Data analysis Matplotlib 3.6.2, SciPy 1.9.3, Seaborn 0.11.2, PyMOL 2.5.0, ForteBio Data Analysis Software Version 9.0.0.14, pycorn 0.19, CryoSparc v4.0.3, Microcal PEAQ-ITC Analysis Software

For manuscripts utilizing custom algorithms or software that are central to the research but not yet described in published literature, software must be made available to editors and reviewers. We strongly encourage code deposition in a community repository (e.g. GitHub). See the Nature Portfolio [guidelines for submitting code & software](#) for further information.

### Data

Policy information about [availability of data](#)

All manuscripts must include a [data availability statement](#). This statement should provide the following information, where applicable:

- Accession codes, unique identifiers, or web links for publicly available datasets
- A description of any restrictions on data availability
- For clinical datasets or third party data, please ensure that the statement adheres to our [policy](#)

Provide your data availability statement here.

## Research involving human participants, their data, or biological material

Policy information about studies with [human participants or human data](#). See also policy information about [sex, gender \(identity/presentation\), and sexual orientation](#) and [race, ethnicity and racism](#).

### Reporting on sex and gender

*Use the terms sex (biological attribute) and gender (shaped by social and cultural circumstances) carefully in order to avoid confusing both terms. Indicate if findings apply to only one sex or gender; describe whether sex and gender were considered in study design; whether sex and/or gender was determined based on self-reporting or assigned and methods used.*  
*Provide in the source data disaggregated sex and gender data, where this information has been collected, and if consent has been obtained for sharing of individual-level data; provide overall numbers in this Reporting Summary. Please state if this information has not been collected.*  
*Report sex- and gender-based analyses where performed, justify reasons for lack of sex- and gender-based analysis.*

### Reporting on race, ethnicity, or other socially relevant groupings

*Please specify the socially constructed or socially relevant categorization variable(s) used in your manuscript and explain why they were used. Please note that such variables should not be used as proxies for other socially constructed/relevant variables (for example, race or ethnicity should not be used as a proxy for socioeconomic status).*  
*Provide clear definitions of the relevant terms used, how they were provided (by the participants/respondents, the researchers, or third parties), and the method(s) used to classify people into the different categories (e.g. self-report, census or administrative data, social media data, etc.)*  
*Please provide details about how you controlled for confounding variables in your analyses.*

### Population characteristics

*Describe the covariate-relevant population characteristics of the human research participants (e.g. age, genotypic information, past and current diagnosis and treatment categories). If you filled out the behavioural & social sciences study design questions and have nothing to add here, write "See above."*

### Recruitment

*Describe how participants were recruited. Outline any potential self-selection bias or other biases that may be present and how these are likely to impact results.*

### Ethics oversight

*Identify the organization(s) that approved the study protocol.*

Note that full information on the approval of the study protocol must also be provided in the manuscript.

## Field-specific reporting

Please select the one below that is the best fit for your research. If you are not sure, read the appropriate sections before making your selection.

Life sciences       Behavioural & social sciences       Ecological, evolutionary & environmental sciences

For a reference copy of the document with all sections, see [nature.com/documents/nr-reporting-summary-flat.pdf](https://nature.com/documents/nr-reporting-summary-flat.pdf)

## Life sciences study design

All studies must disclose on these points even when the disclosure is negative.

### Sample size

n/a

### Data exclusions

n/a

### Replication

n/a

### Randomization

n/a

### Blinding

n/a

## Reporting for specific materials, systems and methods

We require information from authors about some types of materials, experimental systems and methods used in many studies. Here, indicate whether each material, system or method listed is relevant to your study. If you are not sure if a list item applies to your research, read the appropriate section before selecting a response.

## Materials & experimental systems

n/a	Involved in the study
<input checked="" type="checkbox"/>	Antibodies
<input checked="" type="checkbox"/>	Eukaryotic cell lines
<input checked="" type="checkbox"/>	Palaeontology and archaeology
<input checked="" type="checkbox"/>	Animals and other organisms
<input checked="" type="checkbox"/>	Clinical data
<input checked="" type="checkbox"/>	Dual use research of concern
<input checked="" type="checkbox"/>	Plants

## Methods

n/a	Involved in the study
<input checked="" type="checkbox"/>	ChIP-seq
<input type="checkbox"/>	Flow cytometry
<input checked="" type="checkbox"/>	MRI-based neuroimaging

## Plants

### Seed stocks

Report on the source of all seed stocks or other plant material used. If applicable, state the seed stock centre and catalogue number. If plant specimens were collected from the field, describe the collection location, date and sampling procedures.

### Novel plant genotypes

Describe the methods by which all novel plant genotypes were produced. This includes those generated by transgenic approaches, gene editing, chemical/radiation-based mutagenesis and hybridization. For transgenic lines, describe the transformation method, the number of independent lines analyzed and the generation upon which experiments were performed. For gene-edited lines, describe the editor used, the endogenous sequence targeted for editing, the targeting guide RNA sequence (if applicable) and how the editor was applied.

### Authentication

Describe any authentication procedures for each seed stock used or novel genotype generated. Describe any experiments used to assess the effect of a mutation and, where applicable, how potential secondary effects (e.g. second site T-DNA insertions, mosaicism, off-target gene editing) were examined.

## Flow Cytometry

### Plots

Confirm that:

- The axis labels state the marker and fluorochrome used (e.g. CD4-FITC).
- The axis scales are clearly visible. Include numbers along axes only for bottom left plot of group (a 'group' is an analysis of identical markers).
- All plots are contour plots with outliers or pseudocolor plots.
- A numerical value for number of cells or percentage (with statistics) is provided.

### Methodology

#### Sample preparation

In methods

#### Instrument

In methods

#### Software

In methods

#### Cell population abundance

percentages are displayed

#### Gating strategy

Boxes are displayed

Tick this box to confirm that a figure exemplifying the gating strategy is provided in the Supplementary Information.